Air cushioning and bubble entrapment in three-dimensional droplet impacts

PETER D. HICKS and RICHARD PURVIS

Journal of Fluid Mechanics / Volume 649 / April 2010, pp 135 - 163
DOI: 10.1017/S0022112009994009, Published online: 13 April 2010

How to cite this article:
PETER D. HICKS and RICHARD PURVIS (2010). Air cushioning and bubble entrapment in three-dimensional droplet impacts. Journal of Fluid Mechanics, 649, pp 135-163 doi:10.1017/S0022112009994009

J. Fluid Mech. (2010), *vol.* 649, *pp.* 135–163. © Cambridge University Press 2010
doi:10.1017/S0022112009994009

Air cushioning and bubble entrapment in three-dimensional droplet impacts

PETER D. HICKS† AND RICHARD PURVIS
School of Mathematics, University of East Anglia, Norwich NR4 7TJ, UK

(Received 6 June 2008; revised 15 December 2009; accepted 15 December 2009)

Droplet deformation by air cushioning prior to impact is considered. A model is presented coupling the free-surface deformation of a droplet with the pressure field in the narrow air layer generated as a droplet approaches an impact. The model is based upon the density and viscosity in the air being small compared with those in the liquid. Additionally, the Reynolds number, defined using the droplet radius $\mathscr{R}$ and approach velocity $\mathscr{W}_l$, is such that lubrication forces dominate in the air layer. In the absence of significant surface tension or compressibility effects, these assumptions lead to coupled nonlinear integro-differential equations describing the evolution of a droplet free surface approaching a solid wall through air, with or without topography.

The problem is studied numerically with a boundary-element method in the inviscid droplet coupled with a finite-difference method in the lubricating air. In normal impacts, air cushioning will be shown to deflect the free surface upwards, delaying the moment of touchdown and trapping a bubble. The volume of the bubble is found to be $(\mu_g^{4/3}\mathscr{R}^{5/3}/\rho_l^{4/3}\mathscr{W}_l^{4/3})\hat{\hat{V}}$, where μ_g is the gas viscosity and ρ_l is the liquid density and the numerically computed pre-factor $\hat{\hat{V}} = 94.48$. Bubble volumes predicted by this relationship are shown to be in good agreement with experimental observations. In oblique impact or impact with a moving surface with sufficient horizontal motion a bubble is not trapped beneath the approaching droplet. In this case, the region of touchdown is initially crescent shaped with air effects accelerating the moment of touchdown.

1. Introduction

Droplet impacts occur in a wide variety of applications, from ink-jet printing and fluid coating to industrial cooling processes and ice formation on aircraft. Experiments on droplet impacts have found that air bubbles can become trapped near the impact point. The trapping of air during and after impact is a potentially important feature in many of the applications, with the creation of air pockets leading to inconsistencies in the dried coating material or uneven cooling. For higher-speed impacts, acoustic effects generated by the trapped air could generate larger pressures and loads compared with liquid impact alone. The current work focuses on this bubble-trapping process, attempting to enhance the physical understanding of the fluid mechanisms that lead to the air cushioning and entrapment. We also aim to predict likely bubble sizes and clarify the relative importance of the main parameters such as droplet size and impact velocity.

---

† Present address: Department of Mathematics, University College London, Gower Street, London WC1E 6BT, UK. Email address for correspondence: p.hicks@ucl.ac.uk

Experimental evidence of significant air-cushioning effects has been shown by Lesser & Field (1983) and Liow (2001) who demonstrated substantial distortion of a free-surface pre-impact due to cushioning which can also lead to bubble entrapment near the point of impact. High-speed photography has shown air entrapment underneath a droplet impacting a water layer (Thoroddsen, Etoh & Takehara 2003) and a solid (Thoroddsen *et al.* 2005) for droplet radii of order 2 mm. Similar results have been observed in *n*-heptane with equivalent-sized droplets (Chandra & Avedisian 1991) and also in much smaller droplets of radii of 37 μm used in ink-jet printing (van Dam & Le Clerc 2004).

An understanding of pre-impact behaviour is important in developing accurate models of the early stages of post-impact behaviour. Most small-time post-impact models of solid and droplet impacts assume a single point of impact (see for example Korobkin 1997, 1999; Howison *et al.* 2005; Oliver 2002, 2007). Significant air-cushioning effects may delay impact and cause substantial distortion of the free surface and could lead to multiple points of impact and bubble entrapment, none of which is included in current modelling of post-impact behaviour.

A number of authors have considered theoretical models of cushioning behaviour, in particular Smith, Li & Wu (2003) who discussed the relevant literature in detail. Important contributions to physical understanding have been made through inviscid models considered by Wilson (1991), Howison, Ockendon & Wilson (1991), Howison, Ockendon & Oliver (2002) and Korobkin (1997, 1999) and through viscous/inviscid waves examined by King & Tuck (1993), King, Tuck & Vanden-Broeck (1993) and Vanden-Broeck (2001). In a droplet approach with a zero- or low-normal-momentum component, rebound and other non-coalescence behaviours are possible if the initial kinetic energies are transferred into deformation energies by the gas pressure and surface tension forces. Experimentally, these intriguing phenomena have been investigated by Neitzel & Dell'Aversana (2002) and Protière, Boudaoud & Couder (2006). Gopinath & Koch (2002, for rebound) and Smith & Neitzel (2006, for a non-wetting, sliding droplet) analysed these processes, assuming the droplets are deformable and are separated from the impactor by a thin air layer modelled using a lubrication approximation. In higher-momentum violent flows, direct numerical simulations by Gueyffier *et al.* (1999), Josserand & Zaleski (2003) and Mehdi-Nejad, Mostaghimi & Chandra (2003) have captured pre-impact cushioning that could potentially have significant influence on the post-impact development. It should be noted that air entrainment can also occur in post-impact because of the collapse of the impact craters (Prosperetti & Oğuz 1993).

Of most relevance here, Smith *et al.* (2003) examined a fluid layer approaching a wall through a cushioning air film and identified a combined viscous-inviscid effect that balances viscous, lubrication-type forces in the air with a coupled, inviscid response in the droplet. Additionally, they determined a critical Reynolds number based on the droplet diameter, approach velocity, density and viscosity $O(10^7)$, above which the interaction between air and liquid is purely inviscid. In many of the applications described above, the corresponding Reynolds number is $O(10^5)$ or less and the viscous-inviscid model is appropriate. Subsequent work in Purvis & Smith (2004*b*) and Smith & Purvis (2005) applied this subcritical lubricating-air, inviscid-liquid model to high-speed droplets approaching a wall or a liquid film, pre-impact and post-impact, including the influences of surface tension and obliqueness. Mandre, Mani & Brenner (2009) have incorporated compressibility in the air using a modified lubrication equation, while viscous-inviscid interactions for the case of impact between two solid bodies, one or both of which are coated with a shallow liquid layer, has been studied by Korobkin, Ellis & Smith (2008). Vanden-Broeck & Smith (2008) examined the influence of surface tension on the higher-momentum, inviscid-inviscid case.

The previous studies described here have all concentrated on two-dimensional cushioning effects. Our focus is to consider three-dimensional cushioning of a droplet impacting on to a substrate. We investigate pre-impact effects here and adopt the viscous-inviscid limit discussed above, considering a typical Reynolds number that is substantially below the critical value identified in Smith *et al.* (2003). Our fundamental set-up of interest is that of a spherical (or near-spherical) droplet approaching a fixed, impermeable boundary with a thin air layer cushioning the droplet approach. We are looking to understand how the air film causes the free surface to distort during the approach and to capture the associated pressure field, for normal and oblique impacts. We develop the three-dimensional formulation of the air-cushioning problem and investigate the solution numerically, using a combined finite-difference and boundary-integral approach to solve the resulting coupled integro-differential equations.

Reasoning similar to that in the current work applies equally to air cushioning during a solid body impacting on to an otherwise undisturbed liquid layer and as such has implications to the trapping of air pockets under the keel of a ship (see Nethercote, Mackay & Menon 1986; Howison *et al.* 1991) or landslides entering the sea (Ward 2001; Ward & Day 2001). The only difference in the mathematical formulation is that the solid boundary (of known, fixed shape) is now moving with a prescribed velocity, while the far-field requirement on the free surface is that it is horizontal and undisturbed. Other applications include sloshing in liquid natural gas tanks (Miozzi *et al.* 2007) and bubble entrainment in breaking waves (Iafrati 2007).

Section 2 describes the derivation of the three-dimensional governing equations, exploiting the typically small density and viscosity ratios between the air and liquid phases; the air is found to be governed by a lubrication equation and is coupled, via a nonlinear integro-differential equation, with inviscid potential flow in the droplet. Solutions are presented in § 3 for normal impact of spherical droplets. Section 4 extends the analysis to consider oblique impacts, while § 5 considers impact on to a substrate with three-dimensional topography. A final discussion is provided in § 6, which describes the different mechanisms of air cushioning seen in the normal and oblique sections, compares our results with relevant experimental measurements and furthermore briefly describes the physically important extensions of surface tension, of compressibility and of inviscid air cushioning for higher-momentum impacts.

2. Model formulation

As a droplet approaches impact with a solid surface a region of air is trapped between the droplet free surface and the solid (see figure 1). Our aim is to derive a system of equations governing the air cushioning of a droplet impact with a solid surface in three dimensions. We wish to model the evolution of the free surface of the droplet and the pressures in the air layer as impact is approached. The following analysis assumes that the viscosity and density ratios between the two fluids are small, and the influences of surface tension, compressibility and gravity are negligible. We also assume that we are in the below-critical-*Re* regime discussed above so that significant air cushioning does not occur until the air layer is sufficiently thin. The validity of these assumptions is discussed below.

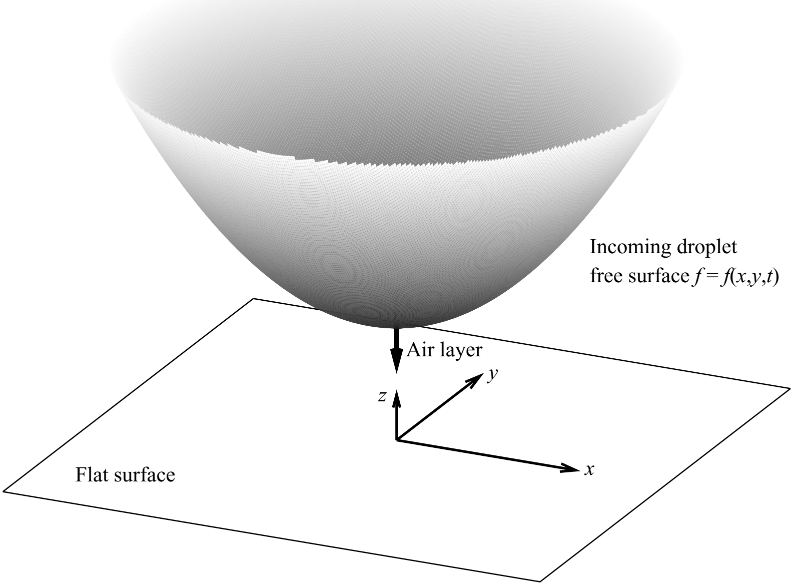

FIGURE 1. An initially spherical droplet approaches impact with a flat surface. The impact is cushioned by the air in the gap between the droplet and the solid.

If we assume an initially spherical droplet of radius $\mathscr{R}$ approaches a wall with constant velocity $(\mathscr{U}_l,\ 0,\ -\mathscr{W}_l)$ in Cartesian coordinates $(X,\ Y,\ Z)$ and does not undergo deformation, then the interface of the droplet is

$$F(X,\ Y,\ T)=-\sqrt{\mathscr{R}^2-(X-\mathscr{U}_l T)^2-Y^2}-\mathscr{W}_l T+\mathscr{R}, \tag{2.1}$$

where the coordinate system is rotated about the vertical Z axis to restrict motion horizontal to the XZ plane. If the wall is located at $Z=0$, then in the absence of air cushioning, the droplet impacts the solid when $T=0$, with initial touchdown $(F=0)$ occurring at $X=Y=0$. When air cushioning is added the droplet will deform with the interface position varying in response to the pressure generated in the narrow gap separating the droplet from the wall. More generally, for a non-spherical droplet, the length $\mathscr{R}$ represents the radius of curvature at the bottom of the droplet.

The droplet radius $\mathscr{R}$ and approach speed $\mathscr{W}_l$ are used to scale distances and fluid velocities, respectively. Non-dimensional displacements are denoted $(\tilde{x},\ \tilde{y},\ \tilde{z})$, while non-dimensional velocities are denoted $(\tilde{u}_\alpha,\ \tilde{v}_\alpha,\ \tilde{w}_\alpha)$, where the subscript $\alpha=l$ (g) in the liquid (gas). The non-dimensional variables are completed with a pressure $\tilde{p}$ and a time $\tilde{t}$ with associated scales $\rho_l\mathscr{W}_l^2$ and $\mathscr{R}/\mathscr{W}_l$, chosen to balance the pressure gradient in each fluid against the inertial terms. The quantity ρ_l represents the density of the liquid droplet, and similarly, ρ_g is used to represent the density of the gas in the air layer. Assuming incompressibility and constant density in both fluids leads to the non-dimensional Navier–Stokes equations

$$\left(\frac{\partial}{\partial\tilde{t}}+\tilde{\boldsymbol{u}}_l\cdot\tilde{\nabla}\right)\tilde{\boldsymbol{u}}_l=-\tilde{\nabla}\tilde{p}_l+\frac{1}{Re}\tilde{\nabla}^2\tilde{\boldsymbol{u}}_l,\quad \tilde{\nabla}\cdot\tilde{\boldsymbol{u}}_l=0, \tag{2.2a}$$

in the liquid and

$$\left(\frac{\partial}{\partial \tilde{t}} + \tilde{\boldsymbol{u}}_g \boldsymbol{\cdot} \tilde{\nabla}\right) \tilde{\boldsymbol{u}}_g = -\frac{\rho_l}{\rho_g}\tilde{\nabla}\tilde{p}_g + \frac{\nu_g}{\nu_l}\frac{1}{Re}\tilde{\nabla}^2\tilde{\boldsymbol{u}}_g, \quad \tilde{\nabla}\boldsymbol{\cdot}\tilde{\boldsymbol{u}}_g = 0, \tag{2.2b}$$

in the air layer. In this expression $\tilde{\nabla} = (\partial_{\tilde{x}}, \partial_{\tilde{y}}, \partial_{\tilde{z}})$; the global Reynolds number for the droplet is $Re \equiv \mathscr{W}_l\mathscr{R}/\nu_l$, and the kinematic viscosities for the liquid and gas are given by $\nu_l = \mu_l/\rho_l$ and $\nu_g = \mu_g/\rho_g$, respectively.

The typical values of the parameters found in applications and recent experiments are worth noting. For example, the experiments by Thoroddsen *et al.* (2005) showing bubble entrapment in droplet impact on to a solid have the Reynolds number Re between 2.5 and 15 000 based on a droplet of radius $\mathscr{R} = 2\,\text{mm}$ and an approach velocity $\mathscr{W}_l$ of up to $= 7\,\text{m}\,\text{s}^{-1}$. The corresponding Weber number $We \equiv \rho_l \mathscr{W}_l^2 \mathscr{R}/\sigma$ is between 10 and 750, where σ is the surface tension coefficient. Experiments with smaller droplets of radius 37 μm by van Dam & Le Clerc (2004) have Re up to $O(10^3)$ and We up to $O(10^2)$. For the higher-velocity impacts found in aircraft icing, droplet radius is in the range 20 μm to 2 mm with a typical droplet approach speed of 60 and $250\,\text{m}\,\text{s}^{-1}$. This corresponds to Reynolds numbers between 100 and 4×10^5 and Weber numbers in the range 100 to 1.6×10^6. In what follows, on the basis of the typically large Weber numbers, we assume that surface tension can be neglected at least in the early stages of droplet deformation where the curvatures are small. For later times, as the curvature of the free surface increases, surface tension effects will become more prominent, but the effect is not investigated here. In all the cases we consider here the Froude number $Fr \equiv \mathscr{W}_l/\sqrt{g\mathscr{R}}$ is large, and thus we neglect gravity in our analysis.

For simplicity, in the current modelling we assume that the air can be treated as an incompressible fluid. Recent work by Mandre *et al.* (2009) has examined a similar model in two dimensions, which includes gas compressibility. They have presented scaling arguments based on the balancing of the gas pressure gradient and droplet deceleration and have concluded that compressibility is significant if

$$\epsilon = P_a\left(\frac{\mu_g}{\rho_l \mathscr{W}_l \mathscr{R}}\right)^{1/3} \ll 1, \tag{2.3}$$

where the ambient pressure $P_a = 10^5$ Pa. For the experiments of Thoroddsen *et al.* (2005), with droplets of radius $\mathscr{R} = 2\,\text{mm}$, gas compressibility becomes important for $\mathscr{W}_l \gg 1.36\,\text{m}\,\text{s}^{-1}$. For the experiments of van Dam & Le Clerc (2004), with droplets of radius $\mathscr{R} = 37\,\mu\text{m}$, gas compressibility becomes important for $\mathscr{W}_l \gg 2.41\,\text{m}\,\text{s}^{-1}$. The results of Thoroddsen *et al.* (2005) give bubble volumes only for impacts at $1\,\text{m}\,\text{s}^{-1}$, and at this speed we are approaching the compressible regime. Similarly, the highest-speed-impact experiments of van Dam & Le Clerc (2004) with $\mathscr{W}_l$ between 10 and $15\,\text{m}\,\text{s}^{-1}$ lie in the regime for which compressible effects are significant. However, given the limited experimental data available, we compare these results with our incompressible model. Additional discussion of compressibility is given in § 6.

In dimensionless variables, the position of the interface of the undisturbed droplet closest to the wall is given by

$$\tilde{f}\left(\tilde{x}, \tilde{y}, \tilde{t}\right) = -\sqrt{1 - \left(\tilde{x} - \tilde{u}_l \tilde{t}\right)^2 - \tilde{y}^2} - \tilde{t} + 1. \tag{2.4}$$

On this interface, we must satisfy the kinematic condition,

$$\frac{\partial \tilde{f}}{\partial \tilde{t}} + \tilde{u}_\alpha \frac{\partial \tilde{f}}{\partial \tilde{x}} + \tilde{v}_\alpha \frac{\partial \tilde{f}}{\partial \tilde{y}} = \tilde{w}_\alpha, \quad \text{on} \;\; \tilde{z} = \tilde{f}\left(\tilde{x}, \tilde{y}, \tilde{t}\right) \;\; \text{for} \;\; \alpha = l \;\; \text{or} \;\; g, \tag{2.5}$$

and a normal stress condition, which in the absence of surface tension implies

$$\tilde{p}_g = \tilde{p}_l. \tag{2.6}$$

Viscosity in the air layer requires the no-slip conditions

$$\tilde{u}_g = \tilde{v}_g = \tilde{w}_g = 0, \quad \text{on} \;\; \tilde{z} = 0. \tag{2.7}$$

2.1. *Liquid droplet and free-surface deformation*

In addition to the radius of the droplet $\mathscr{R}$, a second characteristic local length scale ℓ arises in the problem and corresponds to the horizontal extent over which the pressure in the narrow air gap makes a leading-order contribution to the deformation of the free surface of the droplet. The size of ℓ is determined on the basis of subsequent scaling arguments. However, a small parameter

$$\delta = \frac{\ell}{\mathscr{R}} \tag{2.8}$$

can be defined, corresponding to the aspect ratio of the local length scale to droplet radius. The global Reynolds number in (2.2) must now replaced by a local Reynolds number $Re_l = \mathscr{W}_l \ell / \nu_l = \delta Re$, based on the local length scale ℓ. This local Reynolds number is still typically large for the parameter regime discussed above.

We are primarily interested in water droplets and air; the ratios of gas density to liquid density and gas viscosity to liquid viscosity are approximately 1/772 and 1/100, respectively. Further analysis of the range of applicability of δ and the arguments that follow can be found in Smith *et al.* (2003) and Korobkin *et al.* (2008).

Asymptotic expansions of the fluid velocities and pressures based on the small parameter δ are used to describe the system behaviour close to the point of initial impact, exploiting the small ratios ρ_g/ρ_l and μ_g/μ_l. To study short times and small regions close to the point of impact in the liquid droplet, we rescale

$$(\tilde{x}, \tilde{y}, \tilde{z}) = \delta\,(x, y, z), \tag{2.9a}$$

$$\tilde{t} = \delta^2 t, \tag{2.9b}$$

$$\tilde{f} = \delta^2 f. \tag{2.9c}$$

This motivates asymptotic expansions for the velocity components and pressure in the droplet, of the form

$$(\tilde{u}_l, \tilde{v}_l, \tilde{w}_l, \tilde{p}_l) = \left(u_l, v_l, w_l, \delta^{-1} p_l\right) + \dots, \tag{2.10}$$

where the pressure is scaled in order to match with the high pressure in the air layer.

When these rescalings are applied to the undisturbed free-surface profile (2.4), we recover the far-field behaviour of the droplet interface away from the liquid–air interaction region:

$$f(x, y, t) \sim \tfrac{1}{2}(x - \delta u_l t)^2 + \tfrac{1}{2} y^2 - t + O(\delta), \quad \text{as} \;\; r = \sqrt{x^2 + y^2} \to \infty. \tag{2.11}$$

Here, the term containing the horizontal velocity u_l is separated from the other $O(\delta)$ terms. For oblique impact, unless $u_l = O(\delta^{-1})$, the leading-order system of equations are independent of the horizontal motion and will appear the same as a purely normal impact. The case in which the horizontal velocity is $O(\delta^{-1})$ is considered in § 4.

When the rescalings (2.9) are applied to the kinematic boundary condition (2.5), the free surface satisfies

$$\frac{\partial f}{\partial t} \to w_l, \quad \text{as} \quad z \to 0+, \tag{2.12}$$

to leading order. For $Re_l \gg 1$, (2.2a) implies the leading-order momentum conservation is given by

$$\frac{\partial u_l}{\partial t} = -\frac{\partial p_l}{\partial x}, \tag{2.13a}$$

$$\frac{\partial v_l}{\partial t} = -\frac{\partial p_l}{\partial y}, \tag{2.13b}$$

$$\frac{\partial w_l}{\partial t} = -\frac{\partial p_l}{\partial z}, \tag{2.13c}$$

and the leading-order mass conservation is

$$\frac{\partial u_l}{\partial x} + \frac{\partial v_l}{\partial y} + \frac{\partial w_l}{\partial z} = 0. \tag{2.13d}$$

Hence, we find that the liquid pressure is harmonic. Furthermore, derivatives of pressure are also harmonic, and using an appropriate Green's function we can write a boundary-integral representation for the pressure of the form

$$\frac{\partial p_l}{\partial x}(\boldsymbol{x}, t) = \iint_{\partial\Omega} \left\{ \frac{\partial p_l}{\partial x'}(\boldsymbol{x}', t) \frac{\partial G}{\partial \boldsymbol{n}}(\boldsymbol{x}', \boldsymbol{x}) - G(\boldsymbol{x}', \boldsymbol{x}) \frac{\partial}{\partial \boldsymbol{n}} \left(\frac{\partial p_l}{\partial x'}(\boldsymbol{x}', t) \right) \right\} \mathrm{d}S', \tag{2.14}$$

where $\boldsymbol{x}' = (x', y', z')$ describes the position on the boundary $\partial\Omega$ and $\boldsymbol{x} = (x, y, z)$ describes a point inside $\partial\Omega$. We consider $\partial\Omega$ to be a hemispherical domain in the upper half space and choose a Green's function which decays as $r \to \infty$ and vanishes on the surface $z = 0$. The exact form of the Green's function is given in (A 1). With this choice the contributions to the boundary-integral equation reduce to

$$\frac{\partial p_l}{\partial x}(x, y, z, t) = \frac{z}{2\pi} \int_{-\infty}^{\infty} \int_{-\infty}^{\infty} \frac{p_{x'}(x', y', t)\ \mathrm{d}x'\,\mathrm{d}y'}{\left((x'-x)^2 + (y'-y)^2 + z^2\right)^{3/2}}, \tag{2.15}$$

where $p(x, y, t) = p_l(x, y, 0, t)$ is the pressure on the interface between the droplet and the air and $p_{x'}$ is the derivative of that pressure with respect to the x' coordinate. Note the boundary conditions on the free surface are now applied at $z = 0$, rather than $\tilde{z} = \tilde{f}$, in light of (2.9) as in Smith *et al.* (2003). Using the x-direction momentum equation (2.13a), we can rewrite the left-hand side of this integral in terms of $\partial u_l/\partial t$. If we subsequently differentiate with respect to x, then

$$-\frac{\partial^2 u_l}{\partial x \partial t}(x, y, z, t) = -\frac{3z}{2\pi} \int_{-\infty}^{\infty} \int_{-\infty}^{\infty} \frac{p_{x'}(x', y', t)(x - x')\ \mathrm{d}x'\,\mathrm{d}y'}{((x'-x)^2 + (y'-y)^2 + z^2)^{5/2}}. \tag{2.16}$$

We can generate a similar integral in the y direction by using $\partial p_l/\partial y$ in the boundary integral.

By differentiating the liquid mass continuity equation (2.13*d*) with respect to t and substituting for the integral (2.16) and its equivalent in the y direction, we find

$$\frac{\partial^2 w_l}{\partial z \partial t}(x, y, z, t) = -\frac{3z}{2\pi} \int_{-\infty}^{\infty} \int_{-\infty}^{\infty} \frac{\left[p_{x'}(x', y', t)(x - x') + p_{y'}(x', y', t)(y - y')\right] \mathrm{d}x' \, \mathrm{d}y'}{((x' - x)^2 + (y' - y)^2 + z^2)^{5/2}}. \tag{2.17}$$

We now integrate this boundary integral with respect to z. The result is continuous across the z axis and is evaluated at $z = 0$. The boundary condition at $z = 0$ is used on the left-hand side to give

$$\frac{\partial^2 f}{\partial t^2}(x, y, t) = \frac{1}{2\pi} \int_{-\infty}^{\infty} \int_{-\infty}^{\infty} \frac{\left[p_{x'}(x', y', t)(x - x') + p_{y'}(x', y', t)(y - y')\right] \mathrm{d}x' \, \mathrm{d}y'}{((x' - x)^2 + (y' - y)^2)^{3/2}}, \tag{2.18}$$

a relationship between the free surface and the pressure.

2.2. *Air cushioning*

We now seek a second relationship between the pressure and the free surface based on the behaviour of air in the narrow gap separating the droplet from the solid. The small aspect ratio of the air layer height to the air layer length motivates a rescaling of the length scales in the air layer of

$$(\tilde{x}, \tilde{y}, \tilde{z}) = \delta (x, y, \delta z). \tag{2.19a}$$

Again, we rescale time and the free surface as

$$\tilde{t} = \delta^2 t, \tag{2.19b}$$

$$\tilde{f} = \delta^2 f. \tag{2.19c}$$

Away from the small impact region the droplet is assumed to be unaffected by air cushioning.

In the narrow air gap, the lateral velocities are expected to be large compared with the vertical velocity and scale accordingly to preserve mass conservation; so we obtain the lubrication-type scalings

$$\left(\tilde{u}_g, \tilde{v}_g, \tilde{w}_g, \tilde{p}_g\right) = \left(\delta^{-1} u_g, \delta^{-1} v_g, w_g, \delta^{-1} p_g\right) + \dots, \quad \text{in the air.} \tag{2.20}$$

Substituting into the non-dimensional Navier–Stokes equations in the air layer (2.2*b*), we get the following system of equations governing the leading-order behaviour of the air:

$$0 = -\frac{\partial p_g}{\partial x} + \frac{\partial^2 u_g}{\partial z^2}, \tag{2.21a}$$

$$0 = -\frac{\partial p_g}{\partial y} + \frac{\partial^2 v_g}{\partial z^2}, \tag{2.21b}$$

$$0 = -\frac{\partial p_g}{\partial z} \tag{2.21c}$$

and

$$\frac{\partial u_g}{\partial x} + \frac{\partial v_g}{\partial y} + \frac{\partial w_g}{\partial z} = 0, \tag{2.21d}$$

where we have defined

$$\delta = \left(\frac{\mu_g}{\mu_l \, Re}\right)^{1/3}. \tag{2.22}$$

Note that the inertial and acceleration terms do not appear on the left-hand sides of (2.21*a*)–(2.21*c*), as they are small to leading order compared with the pressure gradient terms, provided that $\mathscr{W}_l^2/\delta^3\mathscr{R} \ll \rho_l\mathscr{W}_l^2/\rho_g\delta^2\mathscr{R}$. In the liquid, we require that the viscous forces (of size $\mu_l\mathscr{W}_l/\rho_l\delta^2\mathscr{R}^2$) are small compared with the acceleration and pressure gradient terms (of size $\mathscr{W}_l^2/\rho_l\delta\mathscr{R}$). Given the definition of δ, we then find

$$\frac{\rho_g}{\rho_l} \ll \delta \ll \left(\frac{\mu_g}{\mu_l}\right)^{1/3}. \tag{2.23}$$

These inequalities ensure the correct matching of time scales and pressures between the assumed inviscid liquid and lubricating air. The first inequality guarantees that inertial and acceleration effects are not present in the lubricating air layer equations to leading order, and the second inequality guarantees that viscous terms are absent in the droplet.

To leading order, the boundary conditions become

$$u_g = v_g = 0, \quad w_g = \frac{\partial f}{\partial t}, \quad \text{on} \quad z = f(x, y, t), \tag{2.24}$$

on the liquid–air interface. No-slip boundary conditions between the air and the solid boundary require

$$u_g = v_g = w_g = 0, \quad \text{on} \quad z = 0. \tag{2.25}$$

The z-direction momentum equation (2.21*c*) and normal stress balance (2.6) imply $p(x, y, t) = p_g(x, y, 0, t)$. Further integration in the air layer, together with the boundary conditions (2.24) and (2.25), gives

$$12\frac{\partial f}{\partial t} = \frac{\partial}{\partial x}\left[f^3\frac{\partial p}{\partial x}\right] + \frac{\partial}{\partial y}\left[f^3\frac{\partial p}{\partial y}\right] = \nabla\cdot\left[f^3\nabla p\right], \tag{2.26}$$

where here, and subsequently, $\nabla = (\partial_x, \partial_y)$ is the two-dimensional gradient operator.

Given suitable far-field conditions, the boundary integral (2.18) and the lubrication-style equation (2.26) constitute a coupled system of integro-differential equations relating interfacial pressure p to the free-surface height f. Before proceeding to solutions we first eliminate the factors of a half from the far-field condition (2.11), to maintain consistency with earlier two-dimensional work by Purvis & Smith (2004*a*). This is done by rescaling the variables with

$$(f, x, y, t, p) = \left(2^{1/3}\bar{f}, 2^{2/3}\bar{x}, 2^{2/3}\bar{y}, 2^{1/3}\bar{t}, 2^{1/3}\bar{p}\right). \tag{2.27}$$

If we immediately drop the overbar, this leaves

$$f(x, y, t) \sim x^2 + y^2 - t, \quad \text{as} \quad r = \sqrt{x^2 + y^2} \to \infty, \tag{2.28}$$

in the far field while leaving the boundary integral (2.18) and the lubrication-style equation (2.26) unchanged. The boundary-integral and lubrication-style equations are numerically solved subject to the far-field boundary condition (2.28) and an initial assumption of constant pressure and an undeformed droplet as $t \to -\infty$.

(*a*) Free-surface

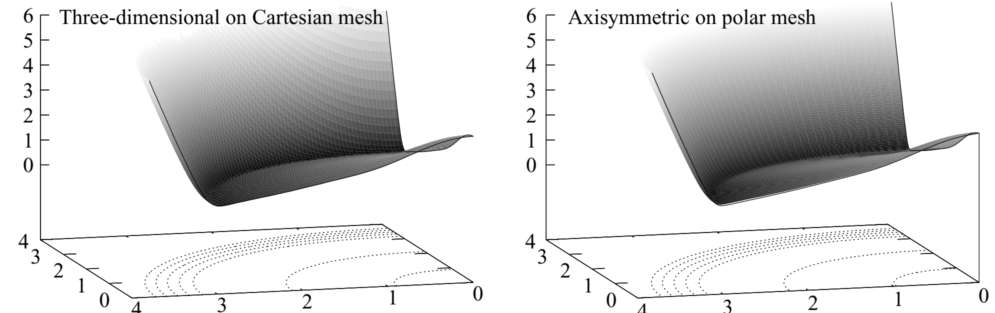

(b) Pressure

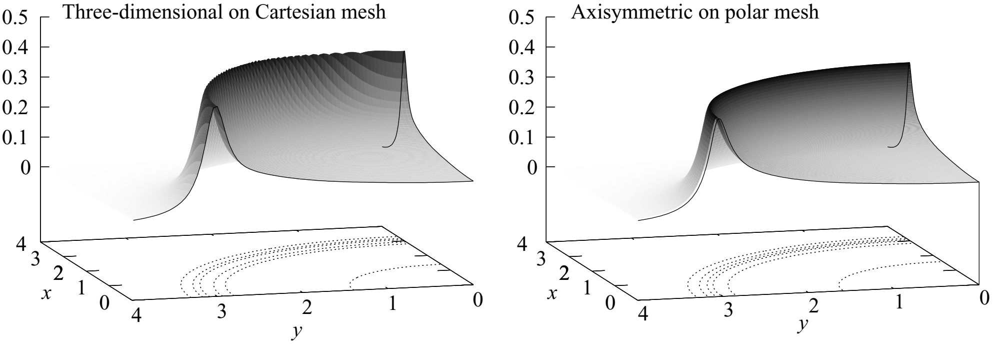

FIGURE 2. (*a*) Free-surface elevation and (*b*) interfacial pressure as a spherical droplet approaches a normal impact with a flat surface for $t = 5$. Minimum (maximum) values of the free surface (pressure) occur on a circle of expanding radius, with the moment of touchdown delayed because of cushioning.

3. Normal impact

We start by considering the cushioning of a spherical droplet as it approaches a flat solid surface. For large negative time the droplet is undeformed (as shown in figure 1), and the pressure in the air gap is zero. The time is scaled such that if the droplet does not deform, then touchdown occurs at $t = 0$. However, air cushioning occurs as the droplet approaches impact, with high pressures in the air gap resisting the motion of the droplet and leading to deformation of the free surface. The evolution of the pressure and free surface continues into positive times prior to the now-delayed impact.

Figure 2 shows one quadrant of (*a*) the free surface and (*b*) the pressure at $t = 5$. The resulting profiles are axisymmetric as expected. Consequently, we can consider the evolution of a droplet from the initially undeformed profile of figure 1 to the deformed profile of figure 2 by looking along just one radius. This is done in figure 3 where (*a*) the free-surface position and (*b*) the pressure are shown at integer increments of time starting at $t = -6$ until touchdown is approached. For large negative times the free surface of the droplet has a global minimum and the pressure has a global maximum, both situated above $x = y = 0$. As time passes the pressure builds up in the air gap and is eventually large enough to deflect the free surface upwards, creating a local maximum above $x = y = 0$. The global free-surface minimum then occurs on a ring at some expanding positive radius away from the bottom of the droplet. The corresponding pressure profiles evolve, with the global pressure maximum flattening and eventually causing a local minimum surrounded by the global maximum pressure which again lies on a ring. The local pressure minimum below the centre of the

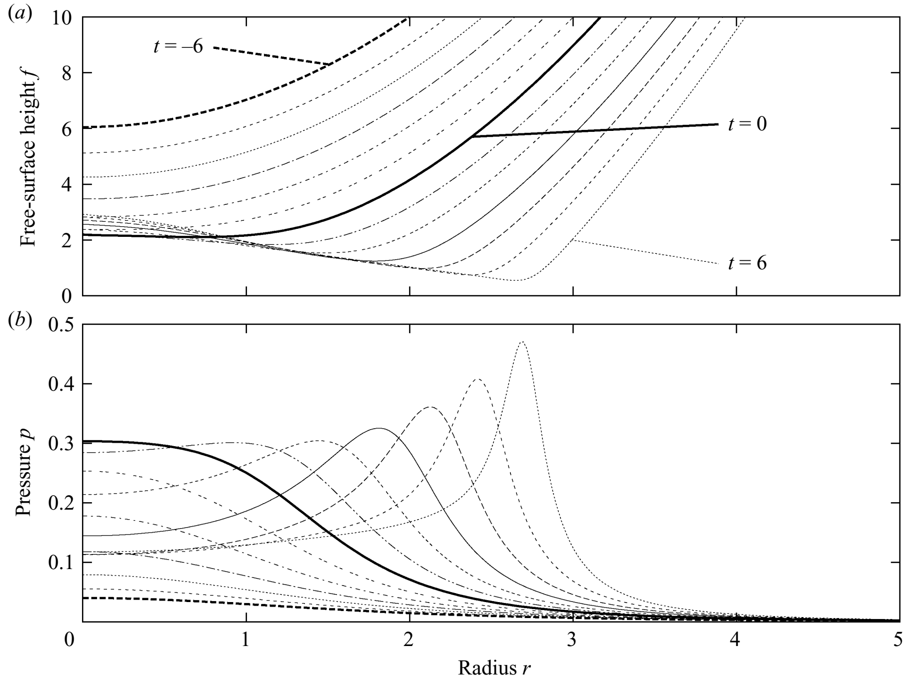

FIGURE 3. (*a*) Free-surface elevation and (*b*) interfacial pressure as a spherical droplet approaches a normal impact with a flat surface. Profiles are axisymmetric and are shown at integer increments of time starting at $t = -6$ until touchdown. In the absence of air cushioning touchdown would occur at $x = y = 0$ when $t = 0$.

droplet remains above the background far-field gas pressure. For larger positive times towards the end of the calculation the ring forming the minimum of the free surface and the ring forming the maximum of the pressure are located at roughly the same radius from the centre of the droplet. The initial touchdown of the droplet on to the free surface will occur along the ring of free-surface minima. Similar free-surface profiles have been measured by Dell'Aversana, Tontodonato & Carotenuto (1997) for a heated silicone–oil droplet pressed against cooled glass through air, where motion is driven by thermocapillary convection due to the temperature difference between the drop and the substrate.

The free-surface deformation traps a pocket of air underneath the centre of the droplet, which, because of the ring of maximum pressure, is prevented from escaping. After impact this pocket of air will then form a bubble trapped within the droplet, like those observed in experiments with water (e.g. Thoroddsen *et al.* 2005). In computations of normal impact, the final instant of touchdown is never reached. However, we can estimate the actual non-dimensional bubble volume $\hat{V}$, by calculating the volume of air trapped within the ring of maximum pressure beneath the incoming droplet. We find $\hat{V} = 29.76$, and this non-dimensional bubble volume is related to the dimensional bubble volume through the scaling of the product of x, y and f. Therefore, the dimensional bubble volume

$$V = \left(\frac{2^5 \mu_g^4 \mathscr{R}^5}{\rho_l^4 \mathscr{W}_l^4} \right)^{1/3} \hat{V} = \left(\frac{\mu_g^4 \mathscr{R}^5}{\rho_l^4 \mathscr{W}_l^4} \right)^{1/3} \hat{\hat{V}}, \tag{3.1}$$

where the factor $2^{5/3}$ appears in light of the rescaling in (2.27) and can be incorporated into an alternative numerical pre-factor $\hat{\hat{V}} = 94.48$. From (3.1), we see that the bubble volume is proportional to $\mathscr{R}^{5/3}$ so that larger droplets trap larger bubbles and is inversely proportional to the approach speed $\mathscr{W}_l^{4/3}$. This confirms the intuitive expectation that a larger droplet traps a bigger bubble because there is a larger free surface which is able to deform and that a faster-approaching droplet traps a smaller bubble because there is less time for the free surface to respond. Dimensional bubble volumes and comparisons to experimental data are discussed in § 6.

4. Oblique impact

In many cases droplets may not undergo normal impact with the substrate. For example, a droplet may approach a surface at an oblique angle, or a droplet of ink in a printing process may impact a rapidly translating substrate. It is computationally expedient to model the latter case, as horizontal motion of the droplet would carry it out of a fixed numerical domain.

We consider an initially axisymmetric droplet impacting a substrate whose velocity is $-\delta^{-1}C$ in order to produce variations from the normal-impact case at leading order. If the velocity of the substrate is aligned with the positive x axis, then the no-slip boundary conditions (2.25) on the substrate now become

$$u_g = -C, \quad v_g = w_g = 0, \quad \text{on} \quad z = 0, \tag{4.1}$$

and the lubrication equation governing flow in the air gap (2.26) is replaced with

$$12\left(\frac{\partial f}{\partial t} + \frac{C}{2}\frac{\partial f}{\partial x}\right) = \frac{\partial}{\partial x}\left[f^3\frac{\partial p}{\partial x}\right] + \frac{\partial}{\partial y}\left[f^3\frac{\partial p}{\partial y}\right] = \nabla\cdot\left[f^3\nabla p\right]. \tag{4.2}$$

The boundary integral equation (2.18) and far-field condition (2.28) on the descending droplet are unaltered by the horizontal motion of the substrate. In results showing impacts with a moving substrate, an initially undisturbed droplet is released at $t = -10$ and the subsequent motion examined. Alternatively, the system of equations governing the cushioning of an oblique droplet can be derived by applying the Galilean transformation $\bar{x} = x + Ct$ to (2.18), (2.28) and (4.2). The resulting system of equations are then the three-dimensional equivalent of the two-dimensional oblique droplet problem studied by Smith, Ovenden & Purvis (2006) and Smith & Purvis (2005). The equations simplify to the normal-impact case in the small-C limit.

Figure 4 shows cross-sectional profiles through the droplet in the plane $y = 0$, parallel to the direction of horizontal motion as a droplet approaches a moving substrate. The free-surface and pressure profiles corresponding to parameter values of $C = -2$, -0.2 and -0.02 are shown, at integer time increments between $t = -9$ and touchdown. From the three sets of profiles it is clear that as $|C|$ increases the time until initial touchdown decreases. This is borne out by figure 5 where the time to initial touchdown is plotted as a function of $|C|$. For values of $|C|$ at the larger end of the range shown, initial touchdown may occur as soon as $t = -6$. However, for $|C| < 0.125$ touchdown occurs after the predicted time if air cushioning is neglected. In all cases the global minimum of the free surface moves away from $x = y = 0$ along the direction of motion of the substrate.

The full three-dimensional free surfaces and pressures at three distinct time steps are shown in figure 6 for $C = -0.2$ and in figure 7 for $C = -0.02$. In both cases, initial touchdown will occur at a point and subsequently spread in an arch round the droplet. For $C = -0.2$ prior to touchdown there is exactly one stationary point

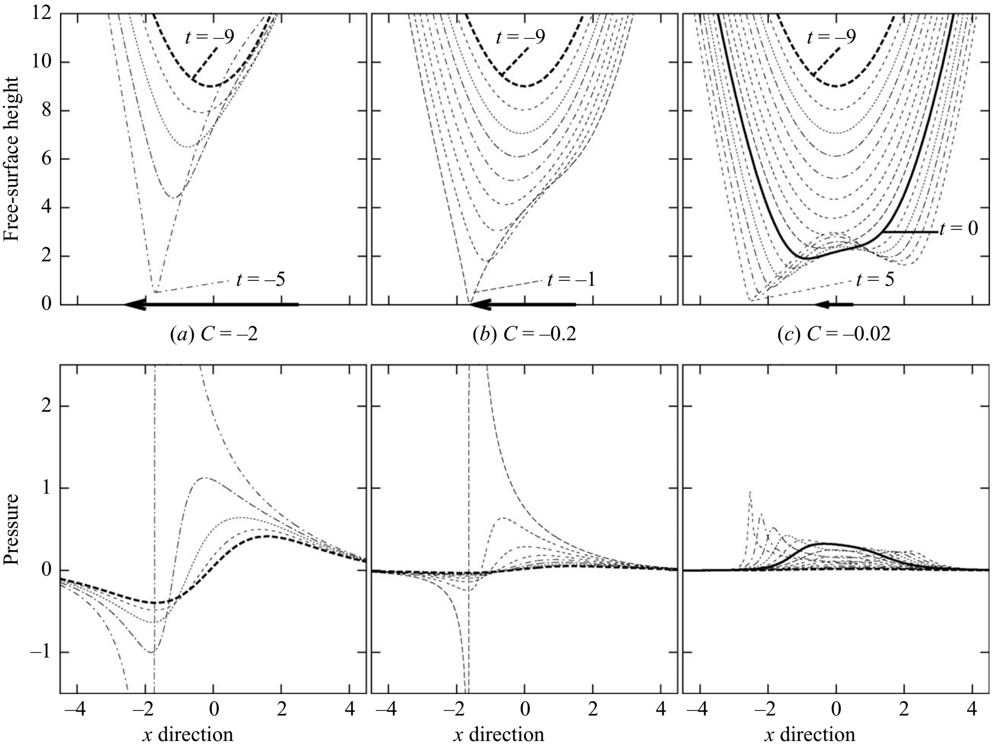

(*a*) $C = -2$ (*b*) $C = -0.2$ (*c*) $C = -0.02$

FIGURE 4. Cross-sectional profiles in the plane $y = 0$ of the free surface (upper panels) and pressure (lower panels) generated by air cushioning a normal droplet impact with a flat substrate moving with speed (*a*) $C = -2$, (*b*) $C = -0.2$ and (*c*) $C = -0.02$. Profiles are shown at integer time step increments starting at $t = -9$ until touchdown. In the absence of air-cushioning effects the free surface would touchdown at $x = y = 0$ at $t = 0$ and would be symmetric about $x = 0$ immediately prior to touchdown.

(a global minimum) on the free surface, right up to the point of touchdown. However, for $t > 1$ in the case $C = -0.02$, two stationary points exist on the free surface: a saddle at the upstream edge of the droplet and a local maximum below the centre of the droplet. These correspond to the second local minimum and the local maximum present in the cross-sectional profiles shown in figure 4(*c*). In figure 7(*a*) at $t = 5$ we see the reappearance of the ring structure which was present in normal impact, albeit with the minima of the ring at different heights on different sides of the ring. As $|C|$ decreases, the ring marking the minima of the free surface flattens to eventually lie in a horizontal plane, and the profiles tend towards their normal-impact counterparts.

At slow substrate speeds, the maximum pressures are generated where the gap between the free surface and the substrate is least, as in the normal-impact case. However, as the speed of the substrate increases, the gas flow becomes driven by the substrate, rather than being dominated by flow in response to incoming droplet. In this regime high pressures are again generated where the gap between free surface and substrate narrows relative to the gas flow. The pressures generated for $C = -0.2$ are significantly greater than those generated for $C = -0.02$. For high substrate speeds downstream of the thinnest gap between free surface and substrate, the expanding flow results in large negative pressures. It is these negative pressures that pull the free surface towards the substrate, hastening touchdown. For $C = -0.02$ regions of

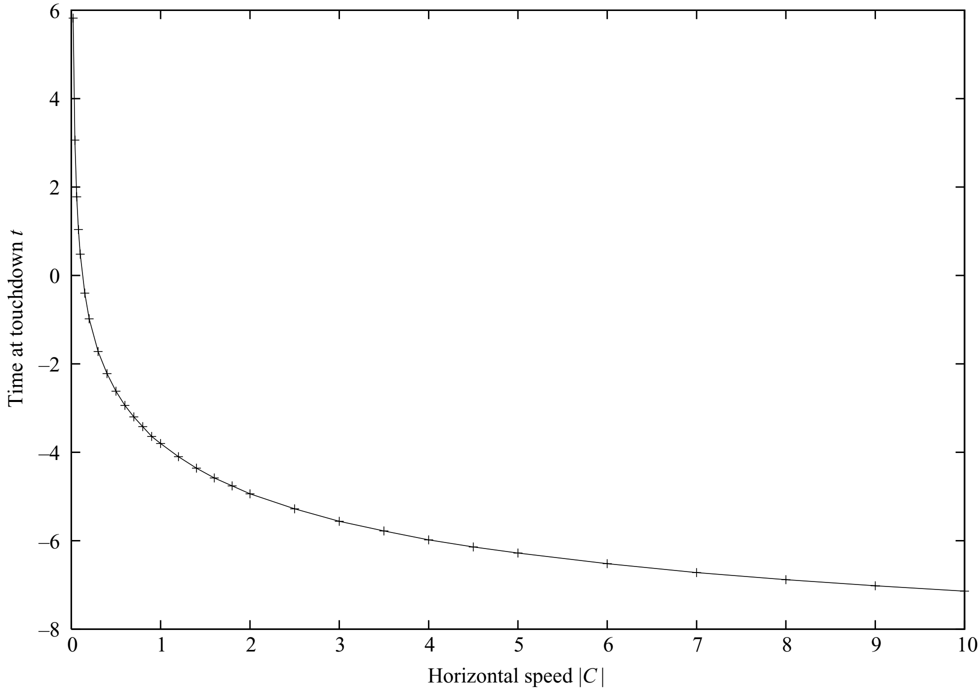

FIGURE 5. Time to initial touchdown as a function of horizontal speed C. Droplets are released from an undisturbed profile with $p = 0$ at $t = -10$.

negative pressure do exist downstream of the free-surface global minimum, but these are not visible on a scale which allows direct comparison with the higher-speed substrate case. With a slowly moving substrate, the ring of free-surface minima and the corresponding ring of pressure maxima may combine to trap a bubble underneath an impacting droplet. However, given substrate motion the full ring on the free surface will not touch down simultaneously. Therefore, bubble entrapment requires the rings of high pressure and low free surface to be maintained post-impact, as the area of the droplet in contact with the substrate spreads in an arch round these rings, from the global free-surface minimum.

In figures 4(a) and 4(b) the global minimum on the free surface accelerates towards touchdown. In all cases numerical evidence suggests that touchdown occurs in finite time. Figure 4(b) shows a case for which the final integer time step is particularly close to touchdown with the free surface reaching zero at one point at $t = -0.96$. This is in marked contrast with our results for normal droplet impacts where, although touchdown is approached, the numerical solution never actually reaches touchdown. Similar predictions are presented in Mandre *et al.* (2009), for a two-dimensional compressible model of normal impact, where an impacting droplet is shown to spread on a thin film of air, rather than touch down. Figure 8 shows a log–log plot of the minimum free-surface height f_{min} against time before touchdown, $t_0 - t$, where t_0 is time to touchdown, for $C = 0$, -0.02, -0.2 and -2. Between $C = -0.02$ and $C = -0.2$ there is a change of curvature, with free-surface minima decelerating as impact is approached for smaller values of $|C|$ and accelerating towards impact for larger values of $|C|$. We have already seen from figure 5 that this

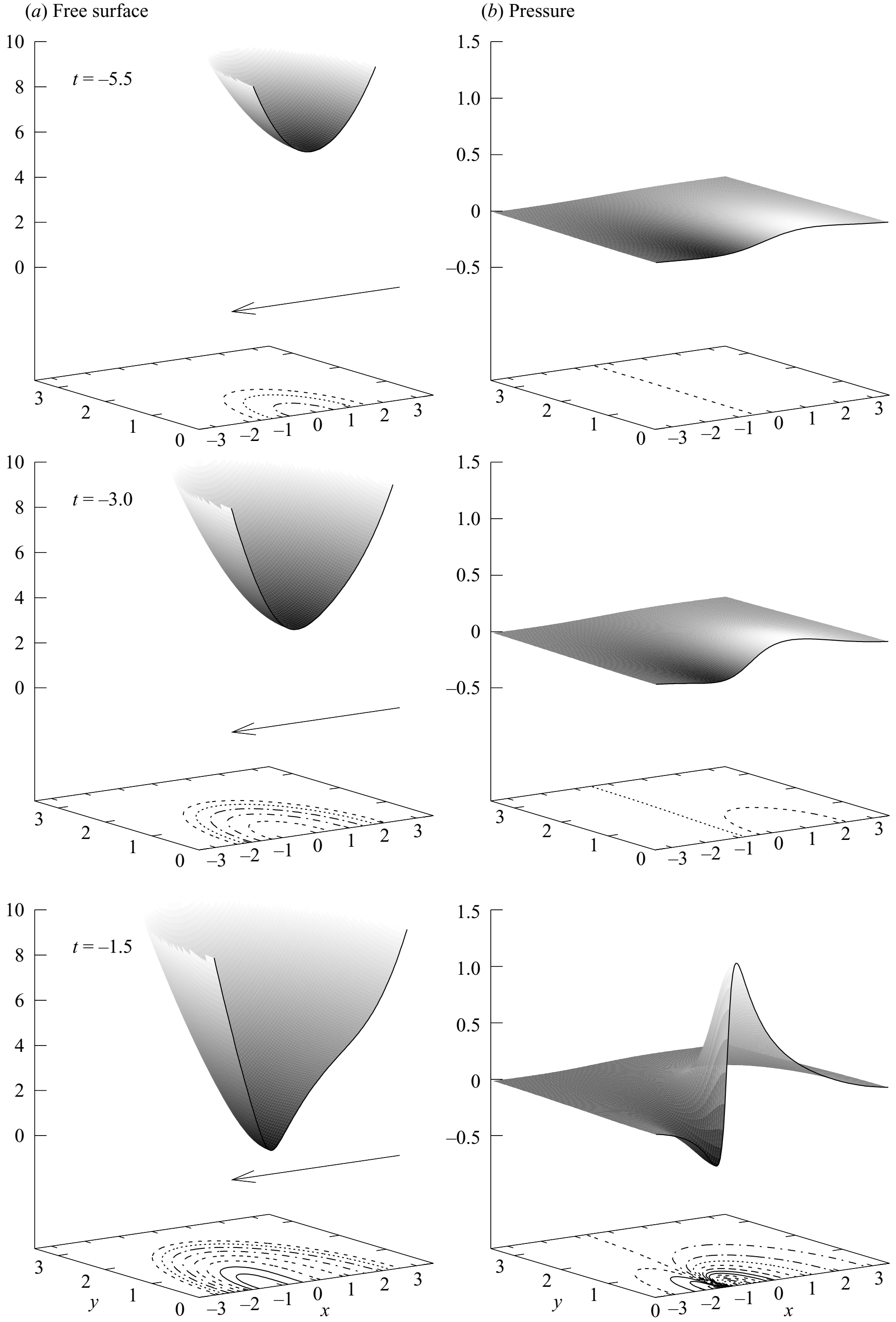

FIGURE 6. The evolution of (a) the free surface and (b) the pressure as a droplet approaches a normal impact with a substrate moving in the direction of the arrow, which corresponds to $C = -0.2$. Profiles are shown at $t = -6.5$, -4 and -0.5.

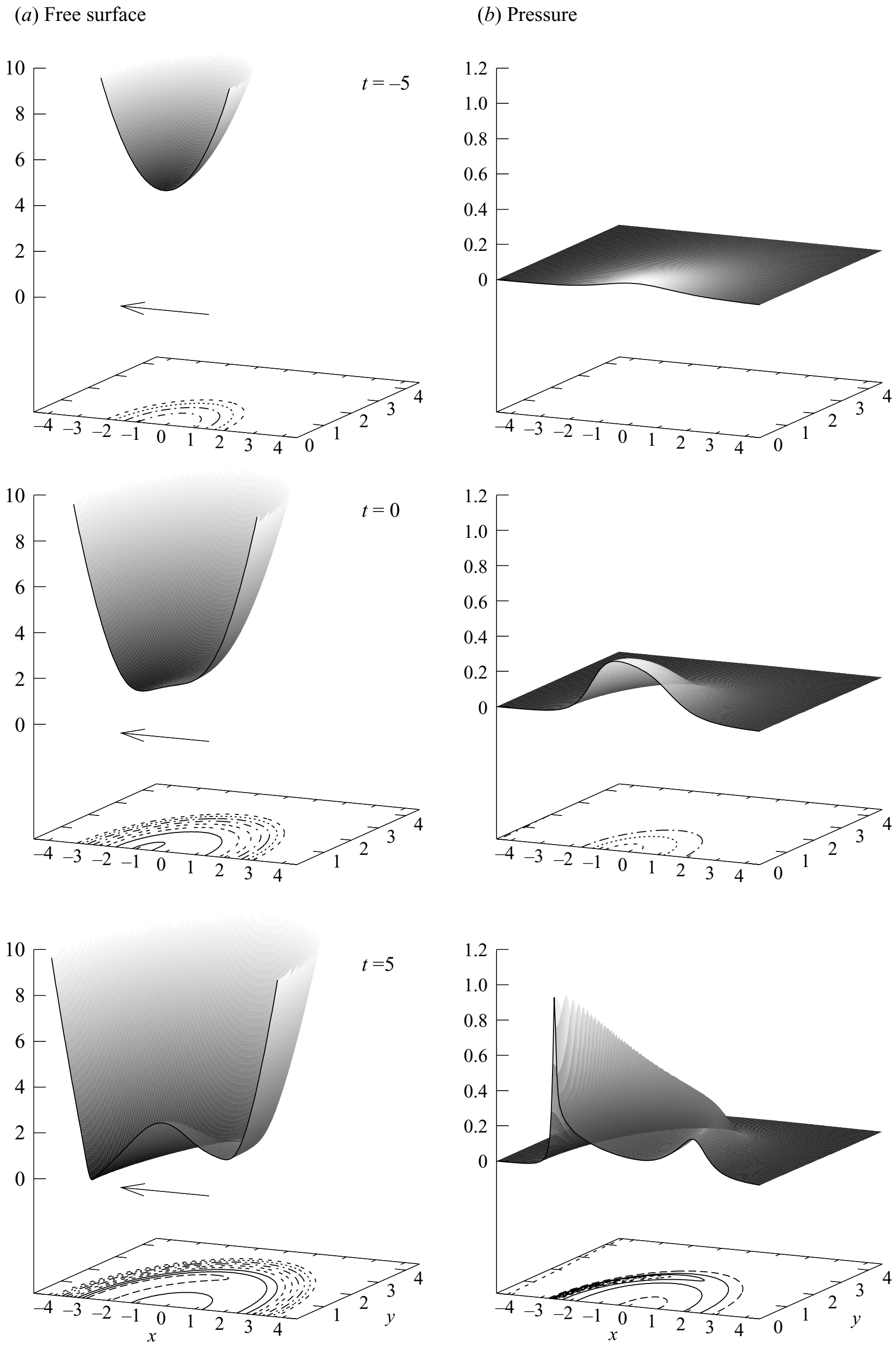
(*a*) Free surface (*b*) Pressure

FIGURE 7. The evolution of (*a*) the free surface and (*b*) the pressure as a droplet approaches a normal impact with a substrate moving in the direction of the arrow, which corresponds to $C = -0.02$. Profiles are shown at $t = -5$, 0 and 5.

transition occurs at $|C| = 0.125$. For $C = 0$, the numerical computation does not reach touchdown, and a nominal t_0 is estimated from the downward velocity of the free surface.

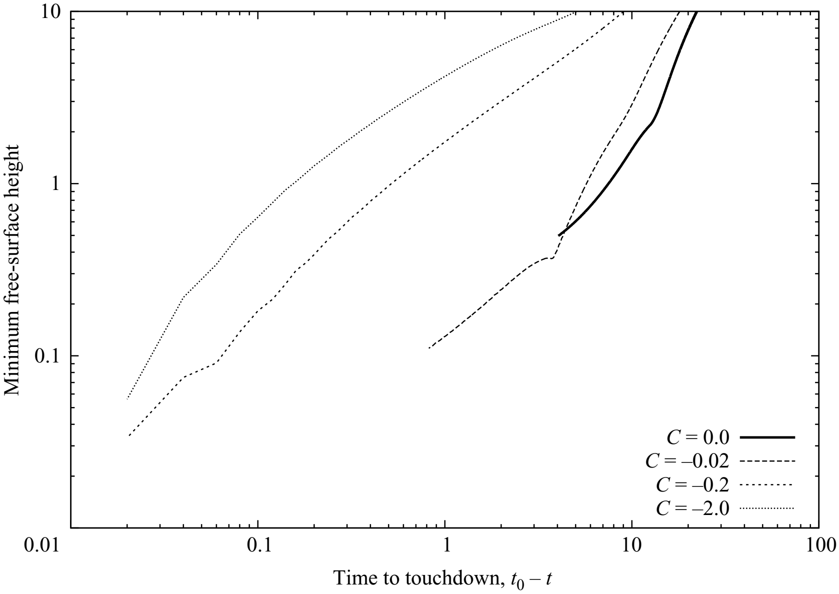

FIGURE 8. The time before touchdown, $t_0 - t$, versus the minimum free-surface height, f_{min}, for $C=0$, -0.02, -0.2 and -2. Here t_0 is time corresponding to the initial touchdown of the droplet.

Of related interest to our oblique impact analysis is the problem of a droplet sliding horizontally over a substrate at moderate to high velocities within a confined channel. In this problem, the experimentally visualized free surface of the droplet measured by Neitzel & Dell'Aversana (2002) has a minimum translated downstream along the direction of tangential motion, which is very reminiscent of our computationally generated profiles for large $|C|$ values (as in figure 6).

5. Normal impact with topography

It is of interest to consider the influence of local topography near impact and how the presence of a roughened surface affects any air cushioning and potential bubble entrapment. This has applications to printing on rough surfaces and in aircraft icing where droplets can impact upon frozen ice shapes. It also has relevance to cushioning of fluid impacts during sloshing in liquid natural gas tanks, where corrugated surfaces are employed to reduce pressures on the tank walls.

We restrict ourselves here to considering surface roughness that is small compared with the droplet size and model this by replacing the flat surface at $z=0$ with some prescribed topography, $z=s(x, y)$. This modifies the no-slip boundary condition at the solid boundary with (2.25) being replaced by

$$u_g = v_g = w_g = 0, \quad \text{on} \quad z = s(x, y). \tag{5.1}$$

With this new boundary condition, the flow in the air gap resulting from a normal droplet impact with this topography satisfies the modified lubrication equation

$$12\frac{\partial f}{\partial t} = \frac{\partial}{\partial x}\left[(f-s)^3\frac{\partial p}{\partial x}\right] + \frac{\partial}{\partial y}\left[(f-s)^3\frac{\partial p}{\partial y}\right] = \nabla\cdot\left[(f-s)^3\nabla p\right], \tag{5.2}$$

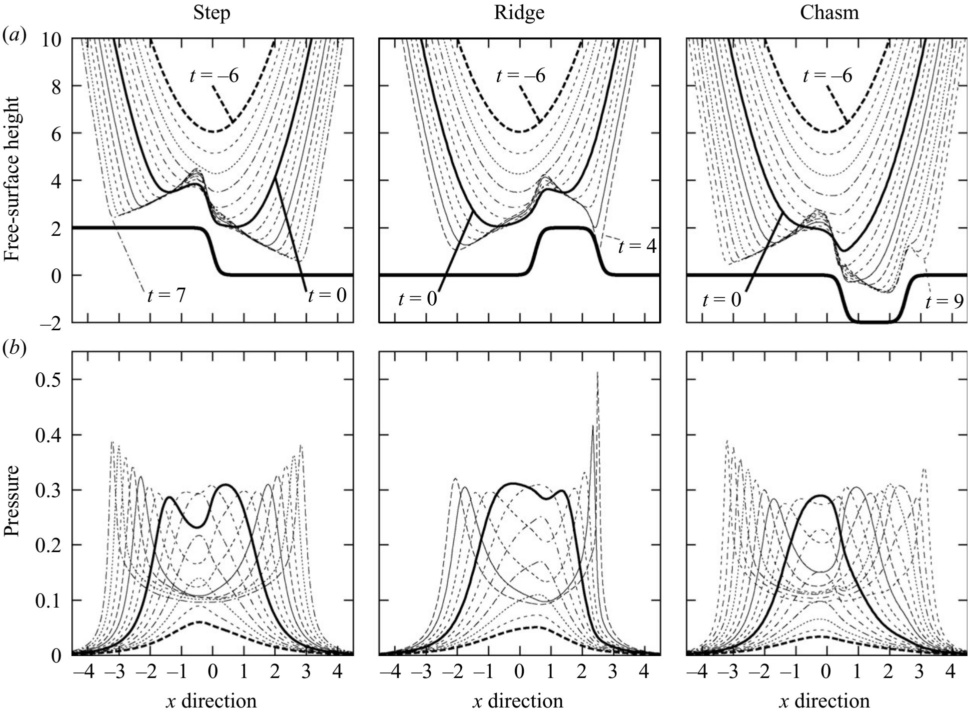

FIGURE 9. (*a*) Free-surface elevation and (*b*) interfacial pressure as a spherical droplet approaches a normal impact with a step topography (left-hand-side panels), a ridge topography (middle panels) and a chasm topography (right-hand-side panels). Profiles are shown at integer increments of time from $t = -6$ until touchdown.

where $s(x, y)$ can be freely prescribed but must satisfy smoothness conditions consistent with the scalings present in the air layer. The boundary integral (2.18) and the far-field condition (2.28) on the droplet remain unaltered.

Three different topographies for surface roughness are considered. These are a step profile with

$$s_s(x, y, \alpha) = 1 - \tanh[5(x - \alpha)], \tag{5.3a}$$

a ridge given by

$$s_r(x, y, \alpha) = \tanh[5(x - \alpha + 1)] - \tanh[5(x - \alpha - 1)] \tag{5.3b}$$

and a chasm given by

$$s_c(x, y, \alpha) = 2 - \tanh[5(x - \alpha + 1)] + \tanh[5(x - \alpha - 1)], \tag{5.3c}$$

where the parameter α moves the position of the topography relative to the droplet. The normal impact of an initially spherical droplet is again considered, with touchdown occurring at $t = 0$ and $x = y = 0$ in the absence of topography and air cushioning. Obviously, with underlying three-dimensional bed topography in the model fully three-dimensional profiles ensue as impact is approached.

Cross-sectional profiles in the plane $y = 0$ for droplet impacts with the step with $\alpha = 0$, the ridge with $\alpha = 3/2$ and the chasm with $\alpha = 3/2$ are shown in figure 9. Profiles are shown at integer time increments between $t = -6$ and touchdown. In regions in which topography on the surface protrudes above the flat plate, the gap between droplet and substrate narrows more rapidly than would occur in impact with a flat plate. This smaller air gap generates a larger pressure, and this acts to deflect the free surface away from the topography. Conversely, in the case of the chasm, the topology results in a larger gap between the substrate and droplet. Here the pressure in the now-wider air gap is less than in the surrounding region, causing the free surface to experience less resistance and move into the chasm. With topography present in the bed, the initial impact may occur at multiple places on each profile, rather than on a coherent ring. The post-impact behaviour for droplet impact with topography with multiple touchdowns is being studied in two dimensions and without air cushioning by Ellis & Smith (2009, personal communication).

Figure 10 shows three-dimensional free surfaces and pressure profiles at the last integer time step calculated for the step with $\alpha = 0$, the ridge with $\alpha = 3/2$ and the chasm with $\alpha = 3/2$. In these figures, away from changes in the topography, the free-surface and pressure isopleths are largely concentric, with the fluid structure locally being two-dimensional. Close to rapid changes in surface topography the flows are fully three-dimensional. One manifestation of the changing topography present in all three pressure profiles is the pressure spike on the ring of maximum pressure, which is located above the point of most rapid change in the surface topography. As the droplet free surface approaches such regions on the bed, the air layer varies over relatively short distances in the azimuthal direction. This variation drives a local, rapidly changing azimuthal pressure gradient and generates significant local velocities. These abrupt changes and relatively large flows give rise to the calculated pressure peaks.

The effect of variation in impact position on one topography shape is investigated by varying the value of α for a ridge modelled by (5.3*b*). Figure 11 shows free-surface and pressure cross-sectional profiles for impact with the ridge topography when $\alpha = 0$, 1, 2, 3 and 4. The effect of the underlying topography is most keenly felt where the variations in the topography are greatest. In regions away from rapid changes in topography, the free-surface and pressure profiles are very similar to those resulting from impact with a flat plate. This culminates with the case $\alpha = 4$, where the variations from the flat-plate case are only visible in the last two profiles, by which point the free surface is very close to the ridge. Variation of the time to touchdown also occurs with changes in the position of topography; touchdown is hastened if the topography lies directly underneath the minimum of the free surface. In this case, the gap separating the topography and free surface is reduced, lessening the time to impact. Variation of the time to touchdown also occurs with changes in the position of topography; touchdown is hastened if the topography lies directly below the point of impact. In this case, the initial gap separating the topography and the free surface is reduced, thereby lessening the time to impact, although the exact local free-surface shapes and hence the touchdown time are dependent on the global shape of the substrate. If we increase the height of the topography, then all the effects of the topography are magnified with the droplet impacting the topography at an earlier time.

6. Discussion

6.1. *Air cushioning*

We have investigated the air cushioning of a droplet impact on to a fixed bed in three dimensions. Through a combination of a lubrication approximation in the air layer and an inviscid description of the droplet behaviour, we have derived a coupled pair of equations governing the evolution of the free surface and pressure field as the

Free surface

Pressure

(*a*) Step, $t = 7$

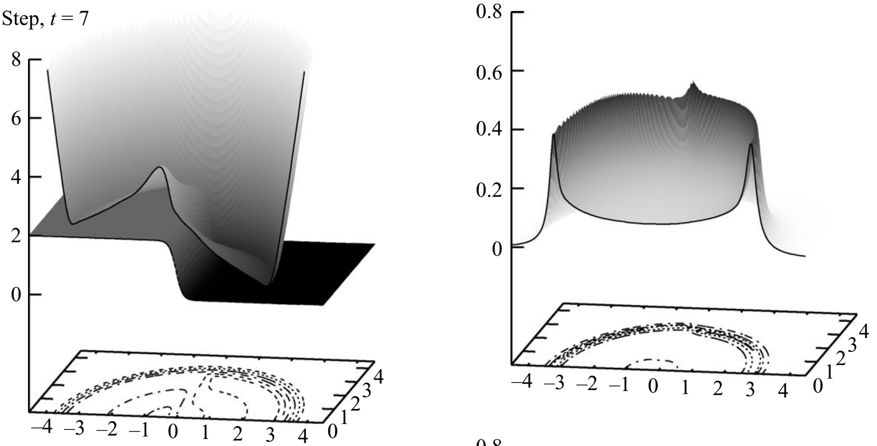

(*b*) Ridge, $t = 4$

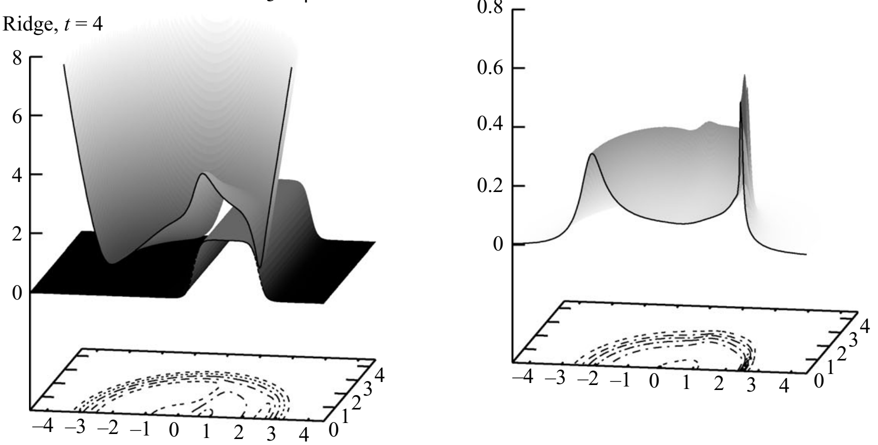

(*c*) Chasm, $t = 9$

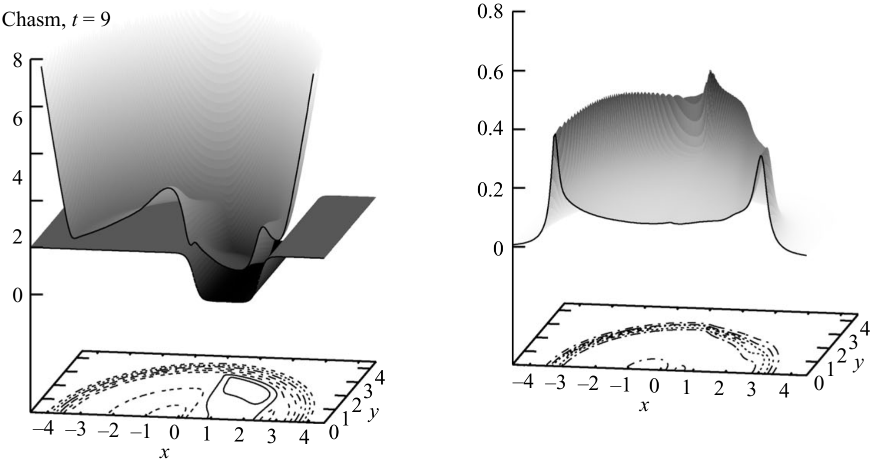

FIGURE 10. The evolution of the free surface (left-hand-side panels) and the pressure (right-hand-side panels) as a droplet approaches a normal impact with (*a*) a step topography at $t = 7$, (*b*) a ridge topography at $t = 4$ and (*c*) a chasm topography at $t = 9$.

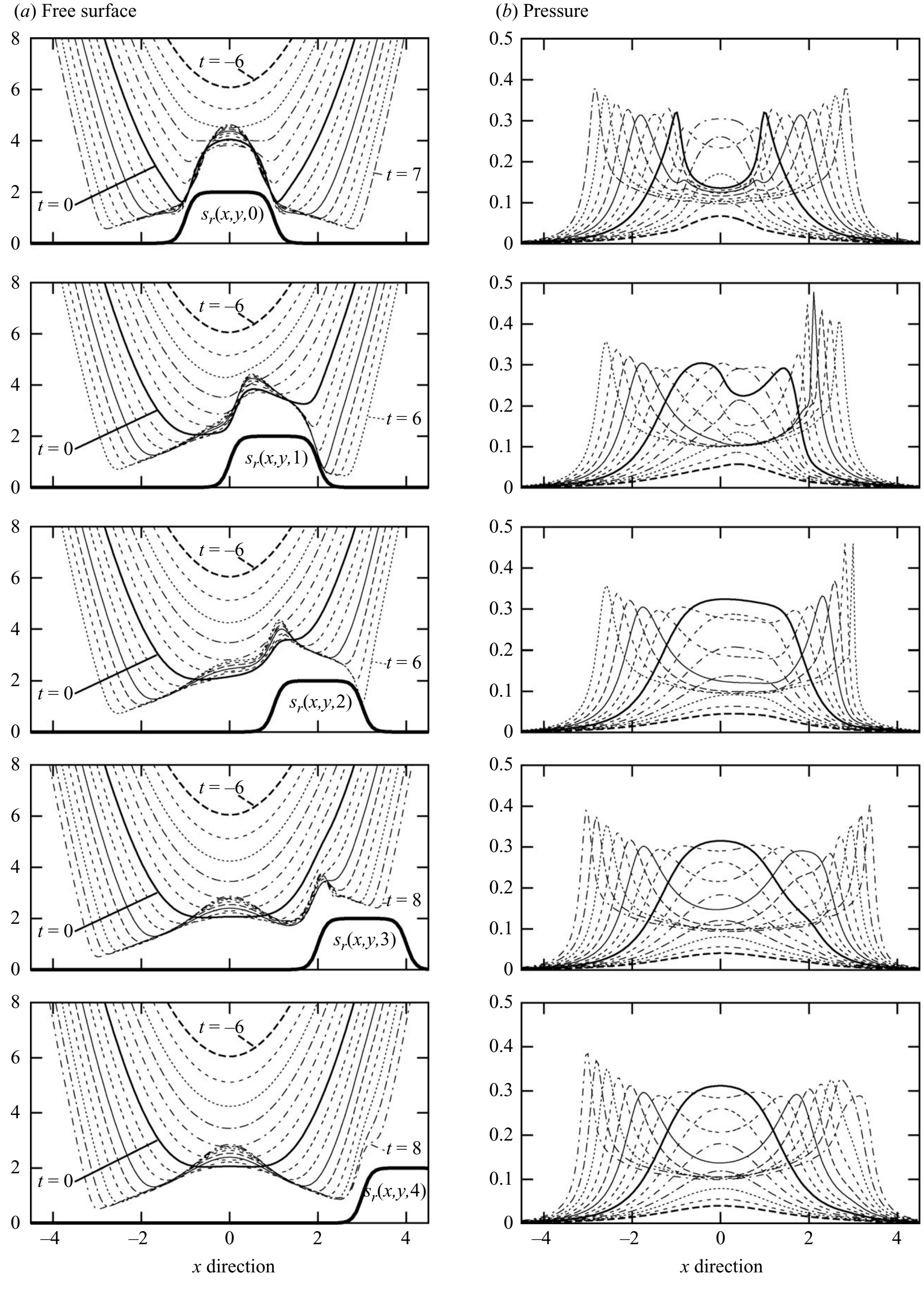

FIGURE 11. The evolution of (a) the free surface and (b) the pressure as a droplet approaches a normal impact with a ridge topography defined by $s_r(x,\ y,\ \alpha)$ as in (5.3b) for $\alpha = 0$, 1, 2, 3 and 4. Profiles are shown at integer increments of time from $t = -6$ until touchdown.

point of impact is approached. Solutions to these equations have been presented for a variety of cases, with the base equations augmented where necessary, to investigate normal and oblique impacts and the effect of underlying topography of the fixed bed. The presence of the cushioning air layer has been shown to have a significant effect on the impact process. In particular, for the case of normal (or near-normal) impact, there is a delay in the touchdown time, while for highly oblique impacts touchdown is hastened.

The upward deflection of the droplet free surface and the resulting delay in impacting the substrate associated with normal impact can be explained through the ideas of squeeze films within classical lubrication theory. In a squeeze film, as two rigid bodies approach each other through a lubricating fluid layer, the pressure in the layer between them increases as the gap is reduced. This is also initially seen in our droplet impacts. As the droplet approaches the substrate the air layer height decreases, and a high-pressure region develops in the narrowest part, as in the traditional squeeze film. This high pressure resists and slows the progress of the droplet, and hence the delay in the moment of touchdown that was found in our results. However, the deformable droplet responds to this pressure increase and does so with an upward deflection of the free surface near the maximum pressure while continuing to advance in regions of lower pressure.

In the case of oblique impact or horizontal motion of the substrate, significant horizontal flow is driven in the lubrication layer. This is now more akin to a roller bearing where, for two rigid bodies in horizontal motion relative to each other, lubrication theory predicts a region of above ambient pressure as the flow is forced into a narrowing gap and a below ambient pressure when the flow is then forced into an expanding gap on the other side of a constriction. As a deformable droplet approaches the substrate it reduces the thickness of the air layer, constricting it near any local minimum of the droplet. The moving substrate is forcing air through the now-constricted gap, and as with the roller bearing, we find a positive-pressure region upstream of the constriction and a negative-pressure region downstream. Upstream of the constriction, the high-pressure region in the air layer resists the progress of the free surface; downstream of the constriction, the negative-pressure region accelerates the free surface towards impact. This acceleration of the free surface into the negative-pressure region carries the minimum downstream and results in the earlier touchdown observed in our results. In between these two extremes of normal and oblique impacts, there is a balance between the motion driven by the descending droplet and the motion driven by the substrate.

6.2. *Comparison with experiments*

It is interesting to compare our predicted trapped air bubble volumes with those observed in experiments that inhabit a similar parameter regime. Experimental results presented by Thoroddsen *et al.* (2005) examine air entrapment by a droplet impacting on to a substrate. Although many of the results presented have corresponding Reynolds numbers Re, which are smaller than those assumed in our asymptotic analysis, some of their experiments, particularly for higher impact velocities, lie within our parameter regime. For these cases, we can compare a predicted trapped droplet size from our model to a measured droplet size in the experiments. For example, Thoroddsen *et al.* (2005) predict that for an incoming droplet radius of 2 mm and approach speed of $1\,\mathrm{m\,s^{-1}}$, the trapped air evolves to a spherical bubble with a radius around 40 μm (see their figure 4a), although the authors comment that the total amount of trapped air is not easily measured. Using our (3.1) with these parameters, we predict a bubble volume trapped by cushioning of 0.182 nl. This corresponds to an equivalent spherical bubble of radius 32.5 μm. Therefore, our model slightly underpredicts the trapped bubble size here. The analysis of Mandre *et al.* (2009) and (2.3) suggests that moderate effects due to compressibility of the gas layer will be present in these experimental results. Additionally, we note that the small Weber numbers in the experiments mean that the role of surface tension is likely to be significant. Even though our model neglects compressibility and surface tension for simplicity, we find reasonable agreement with the experimental results. However, better agreement could be expected through the inclusion of these additional effects.

Thoroddsen *et al.* (2005) also investigated the relationship between the initial horizontal extent of the air disk trapped by the incoming droplet and the radius of curvature at the bottom of the droplet. Their experimental results suggest a linear relationship given by $R_i = (0.16 \pm 0.04)R_{bc}$, where R_i is the initial air disk radius and R_{bc} is the radius of curvature at the bottom of the droplet before impact. In order to investigate the effect of droplet curvature on our model, we note that the dimensional lengths X and Y scale like δR_{bc} where δ has been defined to be proportional to $R_{bc}^{-1/3}$. Therefore, the horizontal lengths scale like $R_{bc}^{2/3}$ and returning to dimensional form gives the relationship between the horizontal extent and the radius of curvature as

$$R_i = \left(\frac{4\mu_g}{\rho_l \mathscr{W}_l} \right)^{1/3} K\, R_{bc}^{2/3}, \tag{6.1}$$

where K is the non-dimensional bubble radius calculated in § 3. We note that rather than a linear relationship we predict that the horizontal extent of the trapped air behaves as $R_{bc}^{2/3}$. For the cases presented in Thoroddsen *et al.* (2005), this corresponds to a predicted relationship of the form $R_i = 0.013 R_{bc}^{2/3}$. As with the bubble volumes above, our model underpredicts the measured air disk radius compared to the Thoroddsen *et al.* (2005) results. For example if we take $R_{bc} = 2$ mm, a typical value for those results, we predict a radius of 0.21 mm while the relationship in Thoroddsen *et al.* (2005) predicts a radius between 0.24 and 0.4 mm. We find better agreement as R_{bc} is reduced within the range of experimental data.

Experiments presented in van Dam & Le Clerc (2004) (see their figure 7), considering the impact of an ink-jet droplet on to a substrate, also show the volume of air bubbles trapped by air cushioning. We see qualitative agreement with their experimental results, particularly the reduction in bubble volume as impact velocity increases. However, for quantitative comparison, only two measurements within their data set (those with highest approach velocity), have a corresponding local Reynolds number which is large and hence have parameter values which fall within the applicability of our model. These points, measured during the impact of droplets with radius 37 μm, have approached velocities of 10 and 13 m s^{-1} and trap bubbles of air of about 0.01 and 0.006 pl, respectively. At these approach speeds, equation (2.3) implies that compressibility in the gas may be significant. However, we shall compare the results to the predictions of our incompressible model.

Figure 12 shows a comparison of our predicted bubble sizes for the given droplet radius and various approach speeds, against the higher velocity experimental data points and model predictions presented in van Dam & Le Clerc (2004). The model presented in van Dam & Le Clerc (2004) is based on the assumption that the pressure gradient is balanced by the viscous forces in the air layer. This balance determines a relationship between the typical air gap height and the radial extent of any significant air cushioning. By further assuming that the local Reynolds number in the air remains

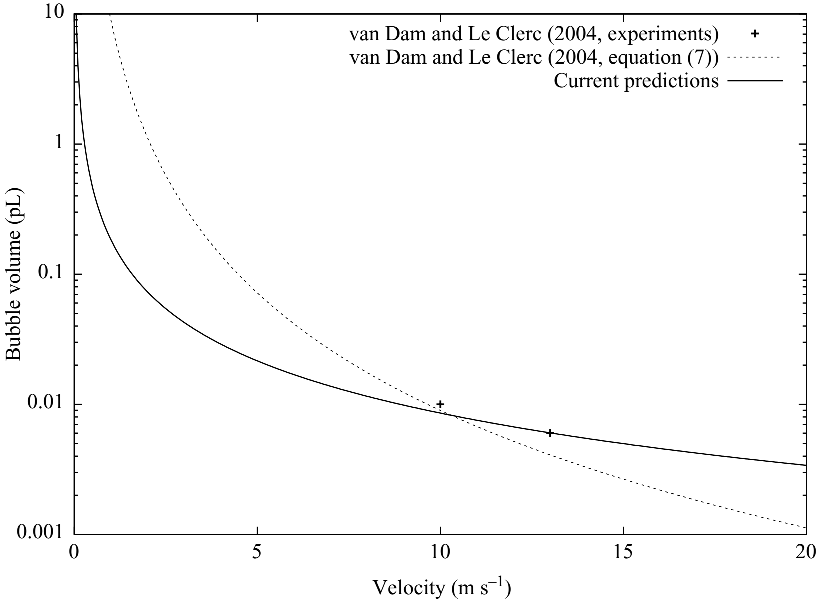

FIGURE 12. A comparison of our bubble volume predictions with the model and experiments of van Dam & Le Clerc (2004). We only include the experimental data points with parameter values that give *Re* within our regime.

fixed as the characteristic gap thickness and approach velocity vary, they can predict how the bubble volume is affected by changes in droplet velocity. Their model predicts that the bubble volume is proportional to $1/\mathscr{W}_l^3$, where $\mathscr{W}_l$ is the approach speed of the droplet. The constant of proportionality is determined from experimental data. In the context of our model, the equivalent assumption would be that the local air Reynolds number, does not vary with approach speed, and again we would predict the same $1/\mathscr{W}_l^3$ behaviour for the bubble volume. However, our predictions have Re_g varying as the approach speed changes. This contrasting approach leads us to predict a bubble volume proportional to $1/\mathscr{W}_l^{4/3}$, where the constant of proportionality is calculated as in § 3.

It can be seen that both our own model and the model of van Dam & Le Clerc (2004) slightly underpredict the measured bubble volumes. The overall predicted trends are very similar, particularly for the higher-momentum droplets where our model is valid. It would be beneficial to have further experimental data points in the higher velocity regime to better validate our predictions. For slower droplet approach speeds our model considerably underpredicts the measured trapped bubble size, so that for a 37 μm radius droplet with an approach speed of around 3 m s^{-1}, the measured volume is 0.18 pl while our prediction is 0.05 pl. The model of van Dam & Le Clerc (2004) better predicts the bubble volumes for these slow approach speeds. However, these impacts have corresponding *Re* up to $O(10^3)$ and in this regime viscous effects may be dominant locally and our scaling arguments are no longer valid in these lower momentum impacts.

For high-speed droplet impacts in aircraft icing, the incoming droplet velocities are much higher than in the above experiments and we predict a maximum trapped bubble volume of the order of 1 pl for a droplet radius of 2 mm and approach speed 60 m s^{-1}; this volume decreases for smaller droplets or higher velocities. Although there is limited experimental data within our parameter range to directly compare to, particularly in the high-speed icing context, it is interesting to note that the predictions of our incompressible and zero surface-tension model are in reasonably good agreement with measured bubble sizes. The neglected surface tension and compressibility are likely to have a significant local effect on the free-surface shape and velocities, particularly as touchdown is approached (see discussion below), but this perhaps is of secondary importance in determining the size of bubble.

6.3. *Extensions*

There are many other physical influences beyond the basic set-up described here. In particular, we have neglected the effect of surface tension in our model based. The scaled surface tension forces are given by

$$\frac{\delta^2}{\rho_l \mathscr{W}_l^2 \ell}\sigma \nabla^2 f = \frac{\delta}{We}\nabla^2 f, \tag{6.2}$$

where σ is the surface tension coefficient and $We = \rho_l \mathscr{W}_l^2 \mathscr{R}/\sigma$, as in § 2. For the violent impacts we are concerned with δ is small and the Weber number We, is typically large and we do not expect surface tension effects to be significant for the majority of the evolution. The exception to this occurs immediately prior to touchdown, when very high curvatures are observed in our predicted free surface. At this stage the large value of $\nabla^2 f$ may compensate for the small coefficient of the surface tension term and latterly in the phase before impact, surface tension may play a role. A study of the two-dimensional situation with surface tension included (Purvis & Smith 2004*a*) suggests that its inclusion can cause a further delay in touchdown, caused in part by the appearance and propagation of waves on the free surface. If the surface tension is relatively small compared with the acceleration, pressure and viscous forces, this delay is shown to occur very close to touchdown. A study of surface tension in a related air-cushioning context by Vanden-Broeck & Smith (2008) (for higher Reynolds numbers than those examined here) have also identified periodic and non-periodic travelling-state solutions that can occur, and it would be of interest to consider a similar approach in the lubrication limit (and three dimensions) considered here.

Compressibility effects in the air could also become significant, especially as the air gap becomes small and the pressures become large. An approximate local Mach number in the air layer is given by the ratio of the local air velocities ($\mathscr{W}_l/\delta$) to the local sound speed ($\sqrt{\gamma P_g/\rho_g}$), where the dimensional gas pressure is given by $P_g = \rho_l \mathscr{W}_l^2/\delta$ and $\gamma = 1.4$ is the ratio of specific heat capacities. This predicts a local Mach number of approximately 0.3, suggesting compressibility can be neglected in the bulk flow. However, larger velocities occur very close to touchdown and therefore it has been suggested (Korobkin *et al.* 2008) that compressibility can be significant even for relatively moderate incoming droplet velocities. In addition to surface tension and compressibility, extending the analysis here to higher-momentum droplets, with the global Reynolds number Re above the critical $O(10^7)$ threshold discussed in the introduction, where the air is essentially inviscid rather than lubricating could be of interest.

The behaviour of the model as touchdown is approached and the thickness of the air layer tends to zero remains an open question. Our numerical results suggest a distinct difference in touchdown behaviour, with finite time touchdown occurring in oblique impacts but not in normal impacts. The two-dimensional calculations of normal impacts by Smith *et al.* (2003) and Mandre *et al.* (2009) also exhibit no numerical evidence that touchdown is reached in finite time. More akin to our oblique case, the Korobkin *et al.* (2008) study of cushioning during normal impacts with shallow liquid layers finds that touchdown does occur within finite time in their numerical results. Further investigation is needed into the mechanisms by which the interface is able to touchdown. Korobkin *et al.* (2008) also present a local self-similar solution that holds as touchdown is approached; while in Smith *et al.* (2003) an analogous self-similar structure is shown to hold if touchdown is assumed to occur in finite time. How these local solutions carry across to the current setting is not clear, especially in the oblique impact case in which behaviour near touchdown is clearly three-dimensional. Analytical investigations into three-dimensional behaviour at impact are currently ongoing.

The authors are very grateful for the support of the EPSRC (EP/E027814/1) and the Nuffield Foundation (NAL/32574).

Appendix. The numerical method

The boundary-integral method used to calculate the free surface of the droplet uses a Green's function which vanishes on $z=0$ and tends to zero in the far field. The explicit form of the Green's function used to calculate (2.18) is

$$G(\boldsymbol{x}', \boldsymbol{x}) = \frac{1}{4\pi\sqrt{(x'-x)^2+(y'-y)^2+(z'-z)^2}} - \frac{1}{4\pi\sqrt{(x'-x)^2+(y'-y)^2+(z'+z)^2}}. \tag{A 1}$$

As is often the case in a boundary-integral method the resulting integral (2.18) is singular at some point on the free surface. In order to overcome these numerical difficulties the boundary integral is desingularized by adding and subtracting the quantity

$$\frac{1}{2\pi}\int_{-\infty}^{\infty}\int_{-\infty}^{\infty}\frac{\left[p_x(x, y, t)(x-x') + p_y(x, y, t)(y-y')\right]\,\mathrm{d}x'\,\mathrm{d}y'}{((x'-x)^2+(y'-y)^2)^{3/2}}, \tag{A 2}$$

so that the numerator is zero at exactly the same points as the denominator. This allows us to evaluate

$$\frac{\partial^2 f}{\partial t^2} = \frac{1}{2\pi}\int_{-\infty}^{\infty}\int_{-\infty}^{\infty}\frac{\left[(p_{x'}-p_x)(x-x') + \left(p_{y'}-p_y\right)(y-y')\right]\,\mathrm{d}x'\,\mathrm{d}y'}{((x'-x)^2+(y'-y)^2)^{3/2}}, \tag{A 3}$$

a double integral over the projection of the free surface on to the wall, where the dependence of (f), $p_{x'}$ and $p_{y'}$ on x, y and t has been suppressed for brevity.

The boundary integral is typically evaluated over the truncated region $x \in [-6, 6]$ and $y \in [-6, 6]$ rather than the doubly infinite limits in (A 3). This truncation is verified by comparing the results generated using this restricted region with the results generated using a larger restricted region. The two sets of results are in good agreement. Solutions are calculated on a regular mesh whose grid points $(x_i, y_j) = (i\Delta x, j\Delta y)$, for $i=-I$ to I and $j=-J$ to J. At the m-time step we write

$$F_{i,j}^m = f(i\,\Delta x, j\,\Delta y, m\,\Delta t) \quad \text{and} \quad P_{i,j}^m = p(i\,\Delta x, j\,\Delta y, m\,\Delta t) \tag{A 4}$$

to be the height of the free surface and the pressure at (x_i, y_j). Simulations are run with $I=J=128$, giving a 257×257 regularly spaced grid.

The position of the free surface and the pressure at the interface are then computed by way of a two-step iterative procedure. Firstly, the lubrication equation (2.26) (or a generalization thereof) is used as a means of calculating an updated pressure field given an initial estimate for the position of the free surface. Secondly, the updated pressure distribution is used in (A 3) to calculate an updated free-surface position. These steps are then repeated until suitable convergence criteria are met. The calculation of the updated pressure in the first step is based on a five-point finite-difference discretization of $\nabla \cdot [f^3 \nabla p]$, coupled with a backward difference discretization of the time derivative, $\partial f / \partial t$. Updated estimates for the new pressure $P^{\star}_{i,j}$ are calculated using a Jacobi update scheme until convergence.

The updated pressure $P^{\star}_{i,j}$ provides a means through which to calculate a new free-surface profile, using (A 3). To derive a second-order temporal discretization of the boundary integral, we first calculate the average of the old pressure and the updated pressure estimate,

$$P^{\star\star}_{i,j} = \tfrac{1}{2}\left(P^{\star}_{i,j} + P^{m}_{i,j}\right). \tag{A 5}$$

This new pressure can be used to find a second-order discretization for an updated free surface of the form

$$\frac{F^{\star\star}_{i,j} - 2F^{m}_{i,j} + F^{m-1}_{i,j}}{(\Delta t)^2} = \frac{1}{2\pi} \sum_{i'=-I}^{I} \sum_{j'=-J}^{J} \left[\frac{W_{i'} W_{j'} \left(A^{\star\star}_{i'j'ij} + B^{\star\star}_{i'j'ij}\right)}{\left(\left(x_{i'} - x_i\right)^2 + \left(y_{j'} - y_j\right)^2\right)^{3/2}} \right], \tag{A 6}$$

where $W_{i'}$ and $W_{j'}$ are appropriately defined quadrature weights on the grid points $\{x_i\}$ and $\{y_j\}$, respectively, and

$$A^{\star\star}_{i'j'ij} = \left[\frac{P^{\star\star}_{i'-1,j'} - P^{\star\star}_{i'+1,j'}}{2\Delta x} - \frac{P^{\star\star}_{i-1,j} - P^{\star\star}_{i+1,j}}{2\Delta x} \right] \left(x_{i'} - x_i\right), \tag{A 7a}$$

$$B^{\star\star}_{i'j'ij} = \left[\frac{P^{\star\star}_{i',j'-1} - P^{\star\star}_{i',j'+1}}{2\Delta y} - \frac{P^{\star\star}_{i-1,j} - P^{\star\star}_{i+1,j}}{2\Delta y} \right] \left(y_{j'} - y_j\right). \tag{A 7b}$$

Trapezium rule weights are used to calculate the value of the integral.

At each new time step the initial estimate for the updated free surface is given by the final free-surface profile calculated during the previous time step albeit with new values for the far-field boundary conditions. Given a sufficiently small time step, typically $\Delta t = 0.02$, this procedure converges with

$$F^{\star\star}_{i,j} \rightarrow F^{m+1}_{i,j} \quad \text{and} \quad P^{\star\star}_{i,j} \rightarrow P^{m+1}_{i,j}, \tag{A 8}$$

subject to a tolerance of 10^{-8} in the root mean square (r.m.s.) error in both the free-surface and pressure profiles between successive iterations. At the start of the calculation, five complete iterative steps are usually sufficient to converge to the new solution at the next time step. Later in the calculation, when the air gap narrows and the free-surface deformations are greatest, the number of iterations increase significantly with perhaps 200 iterations being required by the time $t = 6$, depending on the parameters of the model run. Initially, we release the undisturbed droplet at $t = -8$, with zero pressure in the air gap. Tests with earlier start times show minimal variation from the $t = -8$ case.

To test the accuracy of the numerical method, profiles generated with the full three-dimensional code on a rectangular grid to profiles generated by an axisymmetric version on a polar grid. Figure 2 shows the two sets of numerical results, with the left-hand-side panels calculated using the standard three-dimensional version of the code and the right-hand-side panels calculated using an axisymmetric version of the code on a polar grid with 180 sectors and 513 equally spaced grid points along each radius. The results on the two grids are in good agreement, with the results calculated using the fully three-dimensional version exhibiting no sign of azimuthal instability, although minor defects caused by the Cartesian grid and the plotting routine can be seen along the ring of maximum pressure.

Grid resolution independence was tested by comparing results on a fine grid with $I = J = 128$ with results on a coarse grid with $I = J = 64$. At time $t = 0$, the r.m.s. errors between the free-surface and pressure profiles generated on the coarse grid and on the fine grid are 0.014 and 0.0032, respectively. This indicates that there is a good agreement between the two resolutions and that the profiles are independent of the grid resolution. All of the results we present are calculated using the finer grid. The full three-dimensional code was also used to model the cushioning of an infinite cylinder of liquid; these results showed good agreement with the numerical solutions for the two-dimensional droplet cushioning problem of Smith *et al.* (2003) with r.m.s. errors of the same order as those stated above.

REFERENCES

CHANDRA, S. & AVEDISIAN, C. T. 1991 On the collision of a droplet with a solid surface. *Proc. R. Soc. Lond.* A **432**, 13.

VAN DAM, D. B. & LE CLERC, C. 2004 Experimental study of the impact of an ink-jet printed droplet on a solid substrate. *Phys. Fluids* **16** (9), 3403–3414.

DELL'AVERSANA, P., TONTODONATO, V. & CAROTENUTO, L. 1997 Suppression of coalescence and of wetting: the shape of the interstitial film. *Phys. Fluids* **9** (9), 2475–2485.

GOPINATH, A. & KOCH, D. L. 2002 Collision and rebound of small droplets in an incompressible continuum gas. *J. Fluid Mech.* **454**, 145–201.

GUEYFFIER, D., LI, J., NADIM, A., SCARDOVELLI, R. & ZALESKI, S. 1999 Approximate factorization for time-dependent partial differential equations. *J. Comput. Phys.* **152**, 423–456.

HOWISON, S. D., OCKENDON, J. R. & OLIVER, J. M. 2002 Deep- and shallow-water slamming at small and zero deadrise angles. *J. Engng Math.* **42**, 373–388.

HOWISON, S. D., OCKENDON, J. R., OLIVER, J. M., PURVIS, R. & SMITH, F. T. 2005 Droplet impact on a thin fluid layer. *J. Fluid Mech.* **542**, 1–23.

HOWISON, S. D., OCKENDON, J. R. & WILSON, S. K. 1991 Incompressible water-entry problems at small deadrise angles. *J. Fluid Mech.* **222**, 215–230.

IAFRATI, A. 2007 Air–water interaction in breaking waves. In *Proceedings of the International Conference on Violent Flows* (ed. M. Kashiwagi), vol. VF-2007, pp. 83–93.

JOSSERAND, C. & ZALESKI, S. 2003 Droplet splashing on a thin liquid film. *Phys. Fluids* **15** (6), 1650–1657.

KING, A. C. & TUCK, E. O. 1993 Thin fluid layers supported by surface traction. *J. Fluid Mech.* **251**, 709–718.

KING, A. C., TUCK, E. O. & VANDEN-BROECK, J. M. 1993 Air-blown waves on thin viscous sheets. *Phys. Fluids* A **5**, 973–978.

KOROBKIN, A. A. 1997 Asymptotic theory of liquid–solid impact. *Phil. Trans. R. Soc. Lond.* A **355**, 507–522.

KOROBKIN, A. A. 1999 Shallow water impact problems. *J. Engng Math.* **35**, 233–250.

KOROBKIN, A. A., ELLIS, A. S. & SMITH, F. T. 2008 Trapping of air in impact between a body and shallow water. *J. Fluid Mech.* **611**, 365–394.

LESSER, M. B. & FIELD, J. E. 1983 The impact of compressible liquids. *Annu. Rev. Fluid Mech.* **15**, 97–122.

LIOW, J. L. 2001 Splash formation by spherical drops. *J. Fluid Mech.* **427**, 73–105.

MANDRE, S., MANI, M. & BRENNER, M. P. 2009 Precursors to splashing of liquid droplets on a solid surface. *Phys. Rev. Lett.* **102** (13), 134502.

MEHDI-NEJAD, V., MOSTAGHIMI, J. & CHANDRA, S. 2003 Air bubble entrapment under an impacting droplet. *Phys. Fluids* **15**, 173–183.

Miozzi, M., Lugni, C., Brocchini, M. & Faltinsen, O. M. 2007 The role of the air-entrapment in the flip-through evolution. In *Proceedings of the International Conference on Violent Flows*, vol. VF-2007, pp. 327–335.

Neitzel, G. P. & Dell'Aversana, P. 2002 Noncoalescence and nonwetting behaviour of liquids. *Annu. Rev. Fluid Mech.* **34**, 267–289.

Nethercote, W. C. E., Mackay, M. & Menon, B. 1986 Some warship slamming investigations. *Tech Memo* 86/206. DREA.

Oliver, J. M. 2002 Water entry and related problems. PhD thesis, University of Oxford.

Oliver, J. M. 2007 Second-order wagner theory for two-dimensional water-entry problems at small deadrise angles. *J. Fluid Mech.* **572**, 59–85.

Prosperetti, A. & Oğuz, H. N. 1993 The impact of drops on liquid surfaces and the underwater noise of rain. *Annu. Rev. Fluid Mech.* **25**, 577–602.

Protière, S., Boudaoud, A. & Couder, Y. 2006 Particle–wave association on a fluid interface. *J. Fluid Mech.* **554**, 85–108.

Purvis, R. & Smith, F. T. 2004*a* Air–water interactions near droplet impact. *Eur. J. Appl. Math.* **15**, 853–871.

Purvis, R. & Smith, F. T. 2004*b* Large droplet impact on water layers. *Paper* 2004–0414. AIAA. In *42nd AIAA Aerospace Sciences Meeting and Exhibit*, Reno, NV.

Smith, F. T., Li, L. & Wu, G. X. 2003 Air cushioning with a lubrication/inviscid balance. *J. Fluid Mech.* **482**, 291–318.

Smith, F. T., Ovenden, N. C. & Purvis, R. 2006 Industrial and biomedical applications. In *One Hundred Years of Boundary Layer Research* (ed. G. E. A. Meier, K. R. Sreenivasan & H.-J. Heinemann) pp. 291–300, Proceedings of IUTAM Symposium, Kluwer Academic.

Smith, F. T. & Purvis, R. 2005 Air effects on droplet impact. *Paper* 2005-5184. AIAA. In *4th AIAA Theoretical Fluid Mechanics Meeting*, Toronto, ON, Canada.

Smith, M. K. & Neitzel, G. P. 2006 Multiscale modelling in the numerical computation of isothermal non-wetting. *J. Fluid Mech.* **554**, 67–83.

Thoroddsen, S. T., Etoh, T. G. & Takehara, K. 2003 Air entrapment under an impacting drop. *J. Fluid Mech.* **478**, 125–134.

Thoroddsen, S. T., Etoh, T. G., Takehara, K., Ootsuka, N. & Hatsuki, Y. 2005 The air bubble entrapped under a drop impacting on a solid surface. *J. Fluid Mech.* **545**, 203–212.

Vanden-Broeck, J.-M. 2001 Damped waves generated by a moving pressure distribution. *Eur. J. Appl. Maths.* **12**, 387–400.

Vanden-Broeck, J.-M. & Smith, F. T. 2008 Surface tension effects on interaction between two fluids near a wall. *Quart. J. Mech. Appl. Math.* **61** (2), 117–128.

Ward, S. N. 2001 Landslide tsunami. *J. Geophys. Res.* **100**, 24 487–24 498.

Ward, S. N. & Day, S. 2001 Cumbre Vieja Volcano – potential collapse and tsunami at La Palma, Canary Islands. *Geophys. Res. Lett.* **28** (17), 3397–3400.

Wilson, S. K. 1991 A mathematical model for the initial stages of fluid impact in the presence of a cushioning fluid layer. *J. Engng Math.* **25** (3), 265–285.